NASA/TM–2005–213771

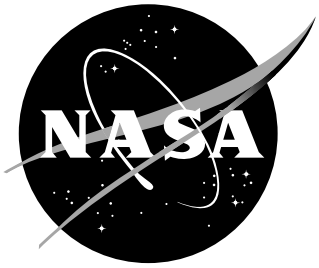

Assessment of an Explicit Algebraic Reynolds Stress Model

Jan-Reneé Carlson
Langley Research Center, Hampton, Virginia

December 2005

The NASA STI Program Office ... in Profile

Since its founding, NASA has been dedicated to the advancement of aeronautics and space science. The NASA Scientific and Technical Information (STI) Program Office plays a key part in helping NASA maintain this important role.

The NASA STI Program Office is operated by Langley Research Center, the lead center for NASA's scientific and technical information. The NASA STI Program Office provides access to the NASA STI Database, the largest collection of aeronautical and space science STI in the world. The Program Office is also NASA's institutional mechanism for disseminating the results of its research and development activities. These results are published by NASA in the NASA STI Report Series, which includes the following report types:

- TECHNICAL PUBLICATION. Reports of completed research or a major significant phase of research that present the results of NASA programs and include extensive data or theoretical analysis. Includes compilations of significant scientific and technical data and information deemed to be of continuing reference value. NASA counterpart of peer-reviewed formal professional papers, but having less stringent limitations on manuscript length and extent of graphic presentations.
- TECHNICAL MEMORANDUM. Scientific and technical findings that are preliminary or of specialized interest, e.g., quick release reports, working papers, and bibliographies that contain minimal annotation. Does not contain extensive analysis.
- CONTRACTOR REPORT. Scientific and technical findings by NASA-sponsored contractors and grantees.
- CONFERENCE PUBLICATION. Collected papers from scientific and technical conferences, symposia, seminars, or other meetings sponsored or co-sponsored by NASA.
- SPECIAL PUBLICATION. Scientific, technical, or historical information from NASA programs, projects, and missions, often concerned with subjects having substantial public interest.
- TECHNICAL TRANSLATION. English-language translations of foreign scientific and technical material pertinent to NASA's mission.

Specialized services that complement the STI Program Office's diverse offerings include creating custom thesauri, building customized databases, organizing and publishing research results ... even providing videos.

For more information about the NASA STI Program Office, see the following:

- Access the NASA STI Program Home Page at ***http://www.sti.nasa.gov***
- E-mail your question via the Internet to help@sti.nasa.gov
- Fax your question to the NASA STI Help Desk at (301) 621–0134
- Phone the NASA STI Help Desk at (301) 621–0390
- Write to:
  NASA STI Help Desk
  NASA Center for AeroSpace Information
  7121 Standard Drive
  Hanover, MD 21076–1320

NASA/TM–2005–213771

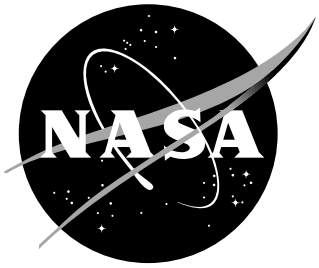

Assessment of an Explicit Algebraic Reynolds Stress Model

Jan-Reneé Carlson
Langley Research Center, Hampton, Virginia

National Aeronautics and
Space Administration

Langley Research Center
Hampton, Virginia 23681-2199

December 2005

The use of trademarks or names of manufacturers in this report is for accurate reporting and does not constitute an offical endorsement, either expressed or implied, of such products or manufacturers by the National Aeronautics and Space Administration.

Available from:

NASA Center for AeroSpace Information (CASI)
7121 Standard Drive
Hanover, MD 21076–1320
(301) 621–0390

National Technical Information Service (NTIS)
5285 Port Royal Road
Springfield, VA 22161–2171
(703) 605–6000

Assessment of an Explicit Algebraic Reynolds Stress Model

This study assesses an explicit algebraic Reynolds stress turbulence model in the in the three-dimensional Reynolds averaged Navier-Stokes (RANS) solver, ISAAC (Integrated Solution Algorithm for Arbitrary Configurations). Additionally, it compares solutions for two select configurations between ISAAC and the RANS solver PAB3D. This study compares with either direct numerical simulation data, experimental data, or empirical models for several different geometries with compressible, separated, and high Reynolds number flows. In general, the turbulence model matched data or followed experimental trends well, and for the selected configurations, the computational results of ISAAC closely matched those of PAB3D using the same turbulence model.

1 Introduction

The capabilities of application–level three–dimensional Reynolds averaged Navier-Stokes (RANS) solvers have increased due to the rapid growth of the speed and the size of computational resources concurrent with advances in turbulence modeling. Requirements of more completely resolving wake–boundary layer flows, highly curved flows and jet shear flow physics, for example, have provided impetus for the implementation of more, higher order, turbulence models into RANS solvers. Two equation turbulence transport models, such as k-ε or k-ω, though a step beyond the previous 0-, 1/2-, and 1-equation models, still make significant compromises in the physical modeling in the flow calculations.

Many current three–dimensional Navier-Stokes methods utilize the higher order turbulence models such as full Reynolds stress model of Launder *et al*;[1] the nonlinear model by Shih, Zhu, and Lumley;[2] and the explicit algebraic Reynolds stress model (EASM) of Gatski and Speziale.[3]These models have had only a minor additional impact to the overall computational effort and, for the most part, have been an improvement over linear eddy viscosity turbulence models.

It is important to be able to evaluate the turbulence models within a numerical code whose numerical characteristics are well-known. In an attempt to quantify potential numerical biases present in the code, a code-to-code comparisons is performed. The challenge is to be sure that the turbulence model is similarly implemented in each code. This level of effort is time consuming but is becoming more essential in the current technical environment where an increasing number of validation studies are undertaken.

[1] B. Launder, G. Reece, and W. Rodi. Progress in the development of a Reynolds stress turbulence closure. *J. Fluid Mech.*, 68:537–566, 1975.

[2] T.-H. Shih, J. Zhu, and J. Lumley. A New Reynolds Stress Algebraic Model. NASA TM–166644, 1994.

[3] T. Gatski and C. Speziale. On Explicit Algebraic Stress Models for Complex Turbulent Flows. *J. Fluid Mech.*, 254:59–78, 1993

The purpose of this paper is to describe and assess the implementation of a particular explicit algebraic Reynolds stress model (EASM) in the RANS solver ISAAC (Integrated Solution Algorithm for Arbitrary Configurations). Earlier results using this model in the solver PAB3D are published in papers by Hamid,[4] and Carlson.[5]

The first two sections briefly describe the ISAAC code and details of the turbulence model equations used herein. The next section contains the validation cases of the EASM simulating four different flows and comparing them with the DNS (Direct Numerical Simulation), empirical or experimental data where appropriate. The last section are N-version tests (code-to-code comparisons) of numerical solutions of ISAAC compared with PAB3D, using two of the four test cases. The nomenclature is found in Appendix A followed by a discussion on turbulence transition indicators used for this study.

[4] K. Abdol-Hamid. Implementation of Algebraic Stress Models in General 3D Navier Stokes Method (PAB3D). NASA CR–4702, December 1995.

[5] J.-R. Carlson. Prediction of High Reynolds Number Flow Using Algebraic Reynolds Stress Turbulence Models, Part 1: Incompressible Flat Plate. *J. Propulsion and Power*, 13:610–619, 1997; and J.-R. Carlson. Prediction of High Reynolds Number Flow Using Algebraic Reynolds Stress Turbulence Models, Part 2: Transonic Shock-Separated Afterbody. *J. Propulsion and Power*, 13:620–628, 1997.

2 Numerical approach

Numerical algorithm

ISAAC [6] is a multiblock, upwind, finite volume code that solves the three-dimensional Favre averaged compressible Navier-Stokes equations with an upwind finite volume formulation. The inviscid terms are upwind-biased spatial differenced and the viscous terms are centrally differenced. This study also uses the flux-difference splitting procedure of Roe[7] with MUSCL[8] (Monotone Upstream-center Scheme for Conservative Laws) differencing and it advances solutions in time with an approximately factored three-factor scheme. The limiter used in the MUSCL scheme was Venkatakrishnan's limiter,[9] unless otherwise noted.

[6] J.H.Morrison. A Compressible Navier-Stokes Solver with Two-Equation and Reynolds Stress Turbulence Closure Models. NASA CR–4440, May 1992.

[7] P. L. Roe. Approximate Riemann Solvers, Parameter Vectors, and Difference Schemes. *J. Comp. Phys.*, 43:357–372, 1981

[8] B. van Leer. Towards the Ultimate Conservative Difference Schemes V. A second Order Sequel to Godunov's Method. *J. Comp. Phys.*, 32:101–136, 1979

[9] V. Venkatakrishnan. Convergence to Steady State Solutions of the Euler Equations on Unstructured Grids with Limiters. *J. Comp. Phys.*, 118:120–130, 1995

k-ε equations transport equations

The transport equations for the turbulent kinetic energy, $\mathrm{k} = \frac{1}{2}\overline{\mathbf{u}'\cdot\mathbf{u}'}$, where $\mathbf{u}'$ is the fluctuating velocity vector, and the turbulent dissipation rate, ε, are[10]

$$\frac{D}{Dt}\left(\overline{\rho}k\right) = \overline{\rho}\mathcal{P}_k - \overline{\rho}\varepsilon + \mathcal{D}_k \tag{1}$$

$$\frac{D}{Dt}\left(\overline{\rho}\varepsilon\right) = \mathrm{C}_{\varepsilon_1}\mathrm{f}_1\frac{\overline{\rho}\varepsilon}{k}\mathcal{P}_k - \mathrm{C}_{\varepsilon_2}\mathrm{f}_2\frac{\overline{\rho}\varepsilon\tilde{\varepsilon}}{k} + \mathcal{D}_\varepsilon \tag{2}$$

with

$$\mathrm{C}_{\varepsilon_1} = 1.44, \quad \mathrm{C}_{\varepsilon_2} = 1.92, \quad \sigma_k = 1.0, \quad \sigma_\varepsilon = 1.3 \tag{3}$$

and where $D/Dt = \partial/\partial t + u_i\partial/\partial x_i$. The equation for the production of turbulent kinetic energy, $\mathcal{P}_k$, uses the Reynolds stresses and the

[10] Several variations of the dissipation rate transport equation exist in the literature. Many of the variations involve the destruction of dissipation term and with the singularity of the term as k approaches zero at the wall. The current model uses the model proposed by Hanjalić and Launder. (K. Hanjalić and B. Launder. Contribution towards a Reynolds-stress closure for low-Reynolds-number turbulence. *J. Fluid Mech.*, 74:593–610, 1976.)

mean flow gradients,

$$\mathcal{P}_k = -\tau_{ij}\frac{\partial u_i}{\partial x_j} \tag{4}$$

The term $\mathcal{D}_k$ derives its form from the turbulent convection and pressure transport terms of the Reynolds stress equations. Often, as is the case presently, the gradient-diffusion model of Daly–Harlow[11] is used resulting in

$$\mathcal{D}_k \;=\; \nabla\cdot\left[\left(\mu+\frac{\mu_t}{\sigma_k}\right)\nabla k\right] \tag{5}$$

The dissipation rate transport equation uses a fully modeled term, $\mathcal{D}_\varepsilon$, for the viscous diffusion and turbulent transport of ε.

$$\mathcal{D}_\varepsilon \;=\; \nabla\cdot\left[\left(\mu+\frac{\mu_t}{\sigma_\varepsilon}\right)\nabla \varepsilon\right] \tag{6}$$

The eddy viscosity, μ_t, in these two transport equations is the high Reynolds number form with the equilibrium model coefficient C_{μ_0},

$$\mu_t \;=\; C_{\mu_0}\frac{\overline{\rho}k^2}{\varepsilon}, \quad C_{\mu_0}=0.09 \tag{7}$$

The functions in the dissipation rate equation are

$$\mathrm{f}_1 \;=\; 1, \quad \mathrm{f}_2 = 1-0.3e^{-{\mathrm{R}_t}^2}, \quad \mathrm{R}_t = \frac{\overline{\rho}k^2}{\mu\varepsilon} \tag{8}$$

and the singularity in the destruction of dissipation term is removed through the term $\tilde{\varepsilon}$

$$\tilde{\varepsilon} \;=\; \varepsilon - 2\nu\left|\nabla\sqrt{k}\right|^2 \tag{9}$$

The boundary conditions enforced on the wall for the turbulence equations are

$$k_{\mathrm{w}} \;=\; 0, \quad \varepsilon_{\mathrm{w}} = 2\nu\left|\nabla\sqrt{k}\right|^2_{\mathrm{w}} \tag{10}$$

Freestream levels for k and ε are derived from the ISAAC user input variables `TKEINF` [12, 13] and `RMUTNF` $\equiv \mu_t/\mu$. `TKEINF` is then nondimensionalized by the square of the speed of sound and used as the freestream value for k. `RMUTNF` determines the freestream value for ε via the expression for the turbulent eddy viscosity.[14] The nondimensional forms designated by the $'$ are then,

$$k'_\infty \;\equiv\; \texttt{TKEINF}\times M^2_\infty = \frac{3}{2}I^2_\infty M^2_\infty \tag{11}$$

$$\varepsilon'_\infty \;\equiv\; \frac{C_\mu\overline{\rho}_\infty k'^2_\infty}{\texttt{RMUTNF}}\left(\frac{\mathrm{R}}{M_\infty}\right) = \frac{C_\mu\overline{\rho}_\infty k'^2_\infty}{(\mu_t/\mu)_\infty}\left(\frac{\mathrm{R}}{M_\infty}\right) \tag{12}$$

[11] B. Daly and F. Harlow. Transport Equations of Turbulence. *Phys. Fluids B*, 11:2634–2649, 1970.

[12] It is interesting to note that if the turbulence intensity is related to the ratio of the turbulent kinetic energy to the mean flow kinetic energy, $\mathrm{I}\sim\sqrt{k/\bar{\mathrm{E}}}$ (where $k=\frac{1}{2}\overline{\mathbf{u}'\cdot\mathbf{u}'}$, $\bar{\mathrm{E}}=\frac{1}{2}\mathbf{U}\cdot\mathbf{U}$), then, assuming in the freestream that $\mathrm{U}^2_\infty = \mathbf{U}\cdot\mathbf{U}$, an expression for the freestream turbulent kinetic energy can be written as $k_\infty \sim \frac{1}{2}\mathrm{I}^2_\infty\mathrm{U}^2_\infty = \frac{1}{2}\mathrm{I}^2_\infty\mathrm{M}^2_\infty a^2_\infty$.

[13] More often, and as is the case for this study, the streamwise turbulence intensity is defined using the streamwise mean and fluctuating velocities as $I\sim\sqrt{\overline{u'u'}}/U$. For isotropic flow k reduces to $\frac{3}{2}\overline{u'u'}$, and again solving for k and expressing the velocity in terms of the Mach number and the freestream speed of sound, results in $k_\infty = \frac{3}{2}I^2_\infty M^2_\infty a^2_\infty$. The difference comes from the definition of I and the method of introducing k back into the equations. Typical levels for I_∞ are approximately 10^{-2} for grid turbulence and 10^{-1} for shear flows. The input variable `TKEINF` is equivalent to $\frac{3}{2}I^2_\infty$.

[14] $\mu_t = C_\mu\frac{\overline{\rho}k^2}{\varepsilon}$, R $\equiv$ Reynolds number per unit length, and $\mathrm{M}_\infty \equiv$ freestream Mach number.

Algebraic Reynolds stress model

One can express the Reynolds stress transport equations in terms of the stress anisotropy tensor $\mathbf{b}\,(=\boldsymbol{\tau}/2k-\mathbf{I}/3)$,

$$\begin{aligned} 2k\frac{D\mathbf{b}}{Dt} &= \frac{D\boldsymbol{\tau}}{Dt}-\frac{\boldsymbol{\tau}}{k}\frac{Dk}{Dt} \\ &= \Big(\boldsymbol{\mathcal{P}}-\frac{\boldsymbol{\tau}}{k}\mathcal{P}_k\Big)+\boldsymbol{\Pi}+\Big(\boldsymbol{\mathcal{D}}-\frac{\boldsymbol{\tau}}{k}\mathcal{D}_k\Big) \end{aligned} \tag{13}$$

where $\boldsymbol{\mathcal{D}}$ represents the combined terms of viscous diffusion and turbulent transport of the Reynolds stresses; $\mathcal{D}_k=\{\boldsymbol{\mathcal{D}}\}/2$ similarly denotes the viscous diffusion and turbulent transport of the kinetic energy equations. The braces, { }, denote a tensor inner product. $\boldsymbol{\Pi}$ represents the stress redistribution tensor, here modeled by the pressure–strain relation developed by Speziale, Sarkar and Gatski (SSG).[15]

$$\begin{aligned} \boldsymbol{\Pi} = &-C_1\varepsilon\mathbf{b}+C_2k\mathbf{S}+C_3k\Big(\mathbf{bS}+\mathbf{Sb}-\frac{2}{3}\{\mathbf{bS}\}\mathbf{I}\Big) \\ &-C_4k\Big(\mathbf{bW}-\mathbf{Wb}\Big) \end{aligned} \tag{14}$$

[15] C. Speziale, S. Sarkar, and T. Gatski. Modeling the pressure-strain correlation of turbulence: an invariant dynamical systems approach. *J. Fluid Mech.*, 227:245–272, 1991.

with the symmetric and antisymmetric strain rate tensors, respectively,

$$\mathbf{S}=\frac{1}{2}\left(\frac{\partial u_i}{\partial x_j}+\frac{\partial u_j}{\partial x_i}\right),\quad \mathbf{W}=\frac{1}{2}\left(\frac{\partial u_i}{\partial x_j}-\frac{\partial u_j}{\partial x_i}\right). \tag{15}$$

The coefficients of the SSG model are denoted C_1-C_4:

$$\begin{aligned} C_1 = C_1^1\frac{\mathcal{P}_k}{\varepsilon}+C_1^0,\quad C_1^0=3.4,\quad C_1^1=1.8, \\ C_2=0.36,\quad C_3=1.25,\quad C_4=0.4 \end{aligned} \tag{16}$$

Similarly, an expression for the production, $\boldsymbol{\mathcal{P}}$, in terms of the tensors, $\mathbf{b}$, $\mathbf{S}$ and $\mathbf{W}$ is,

$$\boldsymbol{\mathcal{P}} = -\frac{4}{3}k\mathbf{S}-2k\,(\mathbf{bS}+\mathbf{Sb})+2k\,(\mathbf{bW}-\mathbf{Wb}) \tag{17}$$

Substituting eqs. (17) and (14) into eq. (13) the implicit anisotropy transport equation is

$$\begin{aligned} 2k\frac{D}{Dt}\mathbf{b} = &\big(-2\mathcal{P}_k-C_1\varepsilon\big)\mathbf{b}-\big(\frac{4}{3}-C_2\big)k\mathbf{S} \\ &-\big(2-C_3\big)k\Big(\mathbf{b}\,\mathbf{S}+\mathbf{S}\,\mathbf{b}+\frac{\mathbf{I}}{3k}\mathcal{P}_k\Big) \\ &+\big(2-C_4\big)k\Big(\mathbf{b}\,\mathbf{W}-\mathbf{W}\,\mathbf{b}\Big)+\Big(\boldsymbol{\mathcal{D}}-\frac{\boldsymbol{\tau}}{k}\mathcal{D}_k\Big) \end{aligned} \tag{18}$$

One can form various models for $\boldsymbol{\mathcal{D}}$, both differential and algebraic, (*e.g.* the gradient-diffusion model of Daly-Harlow[16] or algebraic

[16] B. Daly and F. Harlow. Transport Equations of Turbulence. *Phys. Fluids B*, 11:2634–2649, 1970.

forms that model $\boldsymbol{\mathcal{D}} = f(\boldsymbol{\tau}, \mathbf{b}, \mathcal{D}_k, k)$[17]). The present work uses the algebraic model for the turbulent transport and viscous diffusion by Gatski & Speziale and the solution of the explicit equation by Girimaji.[18] The standard algebraic model for $\boldsymbol{\mathcal{D}}$,[19] eq.(19), is substituted into eq.(18)

$$\boldsymbol{\mathcal{D}} = \frac{\boldsymbol{\tau}}{k}\mathcal{D}_k \tag{19}$$

so that the trailing term is now identically zero. Next, one must derive the expression for the production of turbulent kinetic energy in terms of the anisotropy and symmetric strain rate tensor from one-half the trace of eq. (17),

$$\mathcal{P}_k = \frac{1}{2}\{\boldsymbol{\mathcal{P}}\} = -2k\{\mathbf{bS}\} \tag{20}$$

Substituting in the expression for $\mathcal{P}_k$, eq. (20), and assuming an equilibrium condition of $D\mathbf{b}/Dt = 0$, one writes the implicit equation for the anisotropy tensor,

$$\begin{aligned} 0 = &-\Big(C_1^0 - 2(2 + C_1^1)\{\mathbf{bS}\}\mathrm{T}\Big)\frac{\mathbf{b}}{2\mathrm{T}} - a_1\mathbf{S} \\ &-a_3\Big(\mathbf{b}\,\mathbf{S} + \mathbf{S}\,\mathbf{b} - \frac{2}{3}\{\mathbf{bS}\}\mathbf{I}\Big) + a_2\Big(\mathbf{b}\,\mathbf{W} - \mathbf{W}\,\mathbf{b}\Big) \end{aligned} \tag{21}$$

$$a_1 = \frac{1}{2}\big(\frac{4}{3} - C_2\big), \quad a_2 = \frac{1}{2}\big(2 - C_4\big), \quad a_3 = \frac{1}{2}\big(2 - C_3\big) \tag{22}$$

$$a_4 = \frac{\mathrm{T}}{\gamma_0\dfrac{\mathcal{P}_k}{\varepsilon} + \gamma_1}, \quad \mathrm{T} = \frac{k}{\varepsilon} \tag{23}$$

One can represent the anisotropy tensor by an expansion of a set of basis tensors $\mathbf{T}^{(n)}$ with scalar coefficients α_n as,

$$\mathbf{b} = \sum_{n=1}^{3} \alpha_n \mathbf{T}^{(n)} \tag{24}$$

with

$$\mathbf{T}^{(n)} = \begin{cases} \mathbf{S} & , n = 1 \\ \mathbf{SW} - \mathbf{WS} & , n = 2 \\ \mathbf{S}^2 - \frac{1}{3}\{\mathbf{S}^2\}\mathbf{I} & , n = 3 \end{cases} \tag{25}$$

A basis set of three is able to fully describe two-dimensional flows.[20] Substitution of eq. (24) into eq. (21) results in a cubic equation in scalar coefficient α_1, i.e.,

$$\left(\frac{\alpha_1}{\mathrm{T}}\right)^3 + p\left(\frac{\alpha_1}{\mathrm{T}}\right)^2 + q\left(\frac{\alpha_1}{\mathrm{T}}\right) + r = 0 \tag{26}$$

[17] T. Gatski and C. Speziale. On Explicit Algebraic Stress Models for Complex Turbulent Flows. *J. Fluid Mech.*, 254:59–78, 1993; J.-R. Carlson, N. Duquesne, C. Rumsey, and T. Gatski. Computation of Turbulent Wake Flows in Variable Pressure Gradient. *Computers & Fluids*, 30:161–187, 2001.

[18] S. Girimaji. Fully Explicit and Self-Consistent Algebraic Reynolds Stress Model. *Theoret. Comp. Fluid Dynamics*, 8:387–402, 1996

[19] Most explicit algebraic Reynolds stress models make this assumption for the viscous diffusion and turbulent transport terms, $\boldsymbol{\mathcal{D}} = \boldsymbol{\mathcal{D}}^{\mu} + \boldsymbol{\mathcal{D}}^{t}$, of the stress anisotropy transport equations. A good discussion on algebraic stress models and explicit representations can be found in T. Gatski and T. Jongen. Nonlinear eddy viscosity and algebraic stress models for solving complex turbulent flows. *Progress in Aerospace Sciences*, 36(8):655–682, 2000.

[20] An evaluation of 3- *vs* 5-term basis sets can be found in T. Jongen and T. Gatski. General Explicit Algebraic Stress Relations and Best Approximation for Three-Dimensional Flows. *IJES*, 36:739–763, 1998.

where [21]

$$p = -\frac{\gamma_1}{\eta_1^*\gamma_0} \tag{27}$$

$$q = \frac{1}{\left(2\eta_1^*\gamma_0\right)^2}\left(\gamma_1^2 - 2\eta_1^*\gamma_0 a_1 - \frac{2}{3}\eta_1^* a_3^2 - 2\eta_2^* a_2^2\right) \tag{28}$$

$$r = \frac{\gamma_1 a_1}{\left(2\eta_1^*\gamma_0\right)^2} \tag{29}$$

$$\gamma_0 = \frac{1}{2}\left(C_1^1 + 2\right), \quad \gamma_1 = \frac{1}{2}\left(C_1^0 - 2\right) \tag{30}$$

$$\eta_1^* = \mathrm{T}^2\{\mathbf{S}^2\}, \quad \eta_2^* = \mathrm{T}^2\{\mathbf{W}^2\} \tag{31}$$

[21] The first two invariants of $\mathbf{S}$ and $\mathbf{W}$ are usually defined as $\eta_1 = \{\mathbf{S}^2\}$ and $\eta_2 = \{\mathbf{W}^2\}$, respectively. Some previous articles have used the nomenclature of η^2 ($\equiv \eta_1$) and $\mathcal{R}$ ($\equiv -\eta_2/\eta_1$).

There are three roots to eq. (26) and can be written as,

$$\mathcal{R}_1 = -\frac{p}{3} + 2\sqrt{-\frac{a}{3}}cos\left(\frac{\theta}{3}\right) \tag{32}$$

$$\mathcal{R}_2 = -\frac{p}{3} + 2\sqrt{-\frac{a}{3}}cos\left(\frac{\theta}{3} + \frac{2\pi}{3}\right) \tag{33}$$

$$\mathcal{R}_3 = -\frac{p}{3} + 2\sqrt{-\frac{a}{3}}cos\left(\frac{\theta}{3} + \frac{4\pi}{3}\right) \tag{34}$$

with

$$a = q - \frac{p^2}{3} \tag{35}$$

$$b = 2p^3 - 9q^2 + 27r \tag{36}$$

$$d = \left(\frac{b}{2}\right)^2 + \left(\frac{a}{3}\right)^3 \tag{37}$$

$$\theta = arccos(\phi), \quad \phi = \frac{-b/2}{\sqrt{-a^3/27}} \tag{38}$$

The only physically realizable solution comes from the smallest negative root of the cubic equation. An examination of the equations when $d < 0$ and whether b is either positive or negative reveal that $\mathcal{R}_2$ will always be the smallest negative root using the following logic:

If $d < 0$, $\mathcal{R}_2$ will always be the smallest negative root, therefore

$$\mathrm{C}_\mu^* = -\left(\frac{\alpha_1}{\mathrm{T}}\right) = -\mathcal{R}_2 \tag{39}$$

If $d > 0$, there are two roots,

$$\mathcal{R}_1 = -\frac{1}{3}p + sign\left(-\frac{b}{2} + \sqrt{d}\right)\left|-\frac{b}{2} + \sqrt{d}\right|^{1/3} + sign\left(-\frac{b}{2} - \sqrt{d}\right)\left|-\frac{b}{2} - \sqrt{d}\right|^{1/3} \tag{40}$$

$$\mathcal{R}_2 = -\frac{1}{3}p - \frac{1}{2}sign\left(-\frac{b}{2}+\sqrt{d}\right)\Big|-\frac{b}{2}+\sqrt{d}\Big|^{1/3} - \frac{1}{2}sign\left(-\frac{b}{2}-\sqrt{d}\right)\Big|-\frac{b}{2}-\sqrt{d}\Big|^{1/3} \quad (41)$$

where the model coefficient is

$$\mathrm{C}_\mu^* = -\left(\frac{\alpha_1}{\mathrm{T}}\right) = -min\left(\mathcal{R}_1, \mathcal{R}_2\right) \quad (42)$$

$$\alpha_2 = a_2 a_4 \alpha_1 \quad (43)$$

$$\alpha_3 = -2a_3 a_4 \alpha_1 \quad (44)$$

One then writes the Reynolds stress relation as,

$$\boldsymbol{\tau} = \frac{2}{3}k\mathbf{I} + 2k\alpha_1\,\mathbf{T}^{(1)} + 2k\alpha_2\,\mathbf{T}^{(2)} + 2k\alpha_3\,\mathbf{T}^{(3)} \quad (45)$$

$$= \frac{2}{3}k\mathbf{I} - 2\mathrm{C}_\mu^* k\mathrm{T}\mathbf{S} - \frac{2\mathrm{C}_\mu^* k\mathrm{T}^2}{4\gamma_0\mathrm{C}_\mu^*\mathrm{T}^2+\gamma_1}\Big(a_2\Big(\mathbf{SW}-\mathbf{WS}\Big) - 2a_3\Big(\mathbf{S}^2 - \frac{1}{3}\{\mathbf{S}^2\}\mathbf{I}\Big)\Big) \quad (46)$$

In order to capture the boundary layer log-layer region, one uses the expression $\mathrm{C}_\mu^*\,\mathrm{f}_\mu$ in place of C_μ^* in the linear stress term, making the final expression for the Reynolds stresses

$$\boldsymbol{\tau} = \frac{2}{3}k\mathbf{I} - 2\mathrm{C}_\mu^*\mathrm{f}_\mu k\mathrm{T}\mathbf{S} - \frac{2\mathrm{C}_\mu^* k\mathrm{T}^2}{4\gamma_0\mathrm{C}_\mu^*\mathrm{T}^2+\gamma_1}\Big(a_2\Big(\mathbf{SW}-\mathbf{WS}\Big) - 2a_3\Big(\mathbf{S}^2 - \frac{1}{3}\{\mathbf{S}^2\}\mathbf{I}\Big)\Big) \quad (47)$$

3 Results and Discussion

This section presents four configurations concerning the initial validation of this EASM in the CFD (computational fluid dynamics) code ISAAC.

1. Channel flow DNS at $\mathrm{R}_\tau = 590$.[22]
2. Zero pressure gradient flat plate flow DNS at $\mathrm{R}_\theta = 1410$.[23]
3. Backward facing step experiment.[24]
4. Transonic flow over an axisymmetric afterbody experiment.[25]

This study will also compare solutions utilizing the ISAAC flow solver of the the zero pressure gradient flat plate and the transonic flow over the axisymmetric afterbody with solutions from using the solver PAB3D.

[22] R. Moser, J. Kim, and N. Mansour. DNS of Turbulent Channel Flow up to $\mathrm{Re}_\tau = 590$. *Phys. Fluids*, 11:943–945, 1999.

[23] P. Spalart. Direct Simulation of Turbulent Boundary Layers up to $Re_\theta = 1410$. *J. Fluid Mech.*, 187:61–98, 1988.

[24] D. Driver and H. Seegmiller. Features of a Reattaching Turbulent Shear Layer in Divergent Channel Flow. *AIAA J.*, 23:163–171, 1985.

[25] D. Reubush. Experimental Investigation to Validate Use of Cryogenic Temperatures to Achieve High Reynolds Numbers in Boattail Pressure Testing. NASA TM X–3396, August 1976.

ISAAC validation test cases

Turbulent channel flow at $R_\tau = 590$

DNS data—Computational results from the RANS code will be compared with the numerical experiment (DNS) of Moser *et al.*[26] for a fully developed channel flow at a Reynolds number (Re_τ) of 590. The direct numerical method used a Chebychev-tau formulation in the wall-normal direction and a Fourier representation in the two other directions. The DNS calculation used a third-order Runge-Kutta time discretization for the nonlinear terms, and it applied periodic boundary conditions in the streamwise and spanwise directions. The computational space was dimensioned 384×257×384 with a streamwise length of $2\pi\delta_h$, ($\delta_h \equiv$ channel half-height).

[26] R. Moser, J. Kim, and N. Mansour. DNS of Turbulent Channel Flow up to $\mathrm{Re}_\tau = 590$. *Phys. Fluids*, 11:943–945, 1999.

Computational mesh for ISAAC—The grid consisted of a single block of an H-type mesh topology with the dimensions of 201×201 with the streamwise direction in i and the normal (viscous) direction in j, respectively. Figure 1 shows the one-quarter density grid. The

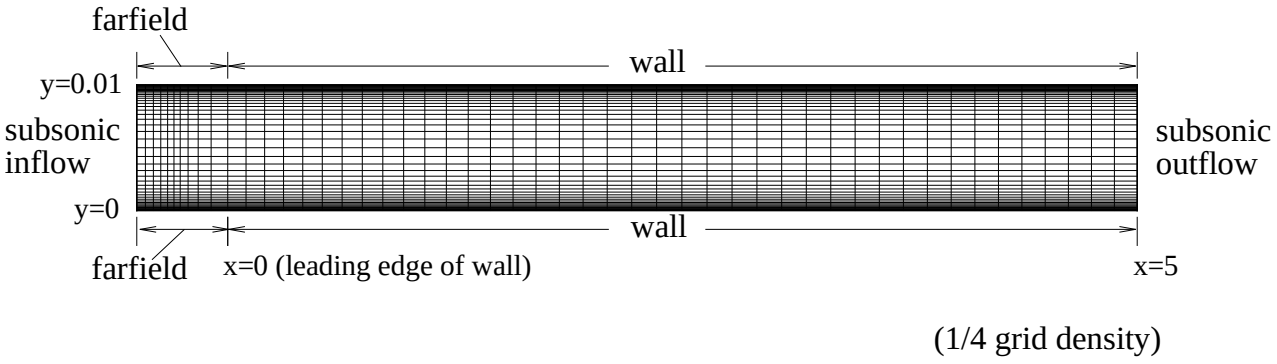

Figure 1: Channel flow computational grid with boundary conditions.

inflow boundary was -0.5 units upstream of the channel entrance. The channel length was 5 units, the channel full height (*i.e.*, from wall to wall) was 0.01 units, and the first grid point away from the wall was at 5.0×10^{-6} units (the first cell center was placed at $y^+ \approx 0.3$) and geometrically stretched away from the wall at a rate of approximately 4 percent. The grid spacing at the channel leading edge was 0.025 units and stretched downstream from the leading edge at a rate of approximately 0.5 percent.

This study applied a 'subsonic inflow' boundary condition to the inflow face $i = 1$, setting the total temperature and total pressure to the input freestream conditions; additionally it applied a 'subsonic outflow' boundary condition to the outflow face $i =$ imax, with the back pressure to the reference static pressure, p/p_∞, set to 1. Since the subsonic inflow boundary cannot immediately abut a no-slip

wall, the first 40 cells of the upper and lower boundaries had a farfield (1-D Riemann invariants) boundary condition imposed.

This study also set the initial freestream turbulent eddy viscosity ratio (`RMUTNF`) to 10, and turbulence intensity (`TKEINF`) to $1.\times10^{-4}$. The freestream Mach number is 0.20, and the Reynolds number per unit grid length is 5.8×10^6 in order to achieve a channel Reynolds number, R_τ, based on the local friction velocity, u_τ, of 590 in the channel. The input unit Reynolds number was manually iterated until the correct R_τ developed in the channel.

Grid density study—This study calculated solutions at four different grid density levels. Each coarser grid was generated by removing every other grid point from the previous level grid.

Figure 2(a) shows the variation with the grid density of the channel Reynolds number versus local Reynolds number.

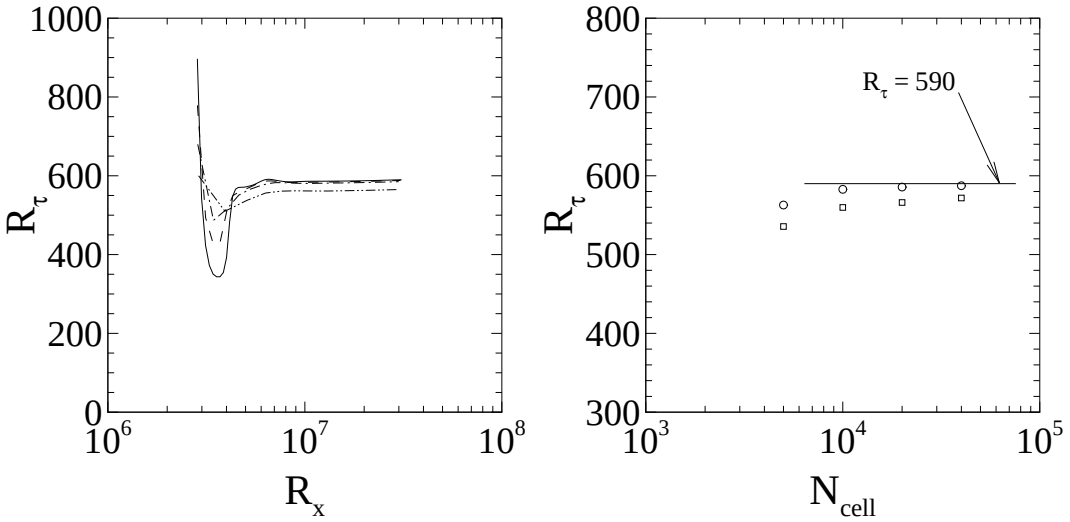

(a) R_τ *vs.* R_x ; ——, Baseline grid ; - - - -, 1/2 grid ; $-\cdot-\cdot-$,(b) R_τ *vs.* N_{cell} ; ○, $R_x = 2.0\times10^7$; □, $R_x = 5.0\times10^6$ 1/4 grid ; $-\cdot\cdot-\cdot\cdot-$, 1/8 grid

Figure 2: Effect of grid density.

With the exception of the region of developing flow ($R_x < 7\times10^6$), the 1/4, 1/2 and baseline grids all result in very similar R_τ distributions. The channel Reynolds number at two streamwise stations, $R_x = 5.0\times10^6$ and $R_x = 2.0\times10^7$ is plotted against the total number of computational cells, fig. 2(b). The channel Reynolds number at each streamwise station in the region of developing flow, $R_x = 5.0\times10^6$, appears to have some local grid sensitivity changing roughly 1 percent between the 1/2 and baseline grids. The channel Reynolds number at the station further downstream at $R_x = 2.0\times10^7$ varies less than 0.3 percent between the 1/2 and baseline grids.

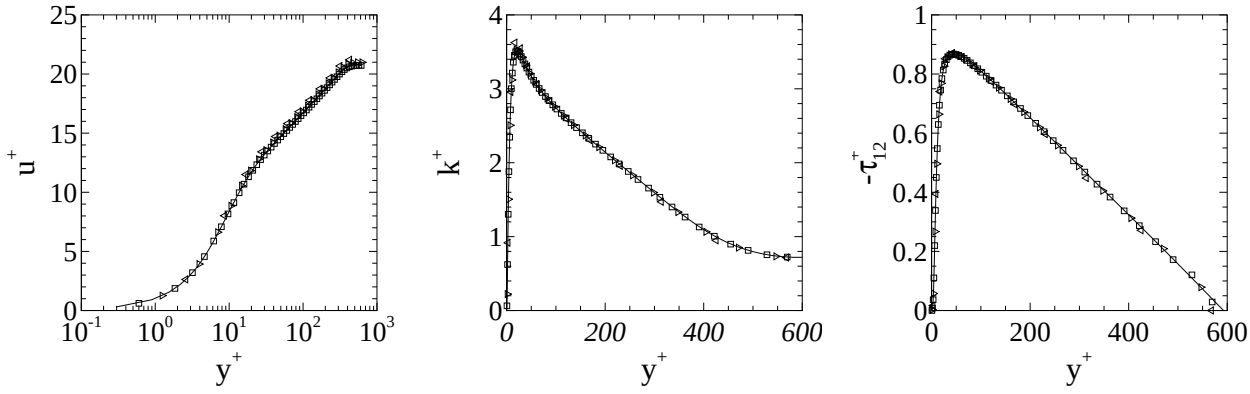

(a) Law-of-the-wall (b) Turbulent kinetic energy (c) Turbulent shear stress

Figure 3: Effect of grid density at $R_\tau = 590$: ——, Baseline grid ($R_\tau = 590$) ; □, 1/2 grid ($R_\tau = 588$) ; ▷, 1/4 grid ($R_\tau = 586$) ; ◁, 1/8 grid ($R_\tau = 565$). .

Mean flow, turbulent kinetic energy, and turbulent shear stress are plotted with grid density in fig. 3. All of the profiles show good grid convergence. Very little shift is observed between solutions generated using the 1/4, 1/2 and baseline grids.

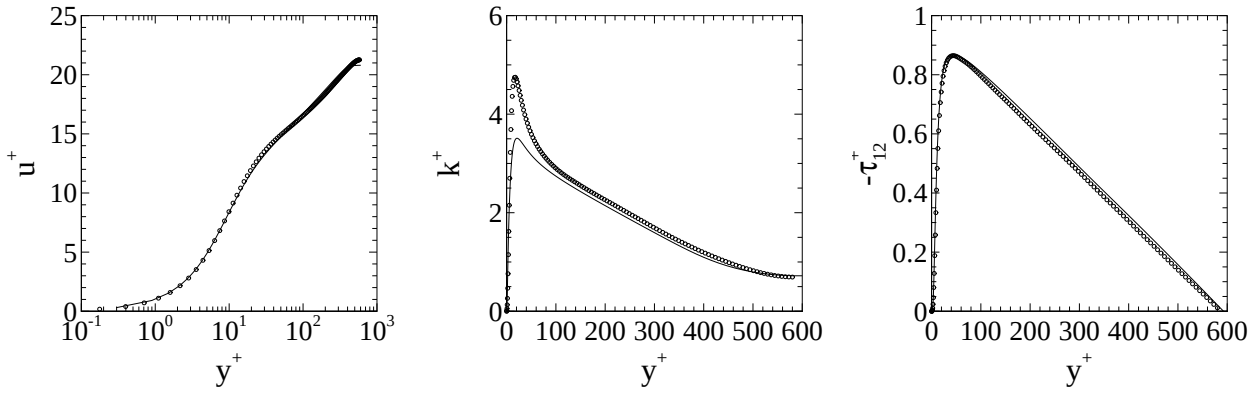

(a) Mean flow (log-linear scale) (b) Turbulent kinetic energy (c) Turbulent shear stress

Figure 4: Comparisons with DNS at $R_\tau = 590$, linear scale. ——, EASM; ○, DNS [Moser, Kim & Mansour].

EASM comparisons with DNS—Figures 4–7 show an evaluation of the EASM for predicting mean and turbulent flow characteristics of the channel flow. In general, there is good agreement between the EASM and the DNS data, with the exception of the anisotropy of the normal stresses approaching the wall and the channel centerline.

The normal Reynolds stresses are equal to 2/3 k with linear two-equation eddy viscosity turbulence models. The pressure-strain relation in the Reynolds stress transport equation (the basis for the EASM) can redistribute turbulent kinetic energy between the

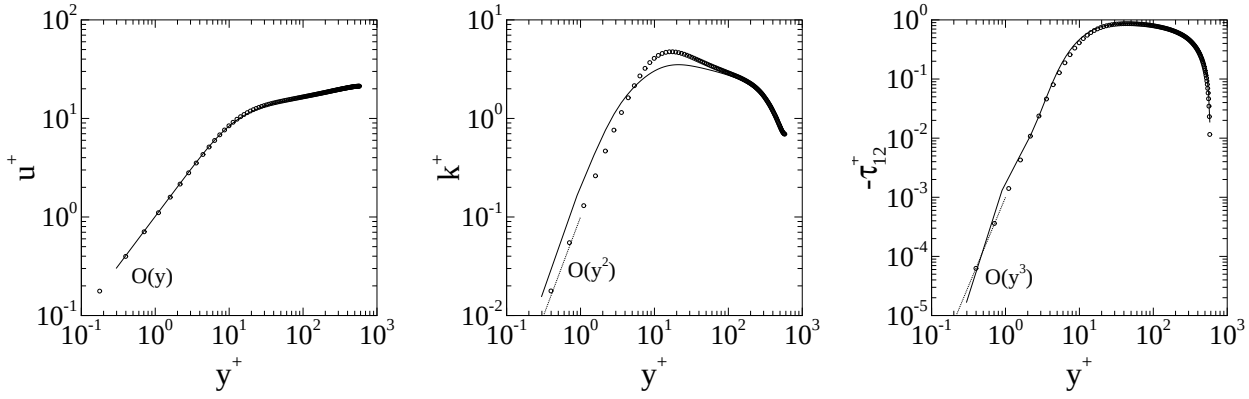

(a) Mean flow (b) Turbulent kinetic energy (c) Turbulent shear stress

Figure 5: Comparisons with DNS at $R_\tau = 590$, log-linear scale. ——, EASM; ○, DNS [Moser, Kim & Mansour].

different stress components resulting in anisotropy in the flow as one may observe in figs. 6a and 6b. Though in the region approaching

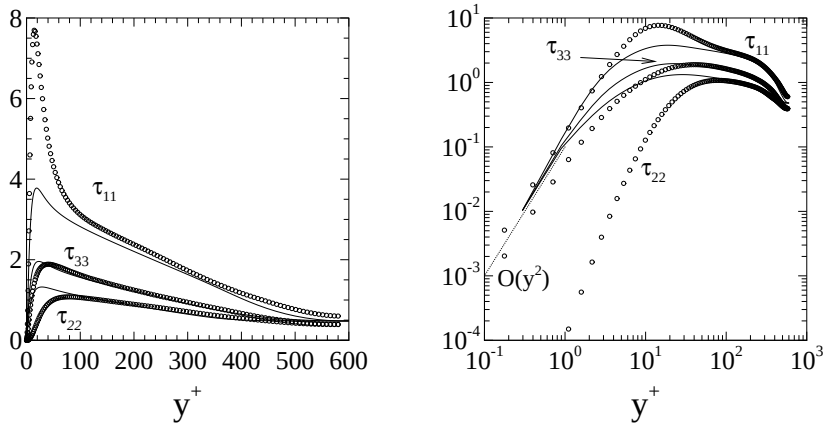

(a) Linear scale (b) Log-log scale

Figure 6: Comparisons with DNS at $R_\tau = 590$, turbulent normal stresses. ——, EASM; ○, DNS [Moser, Kim & Mansour].

the wall, the stress anisotropy due to the presence of the solid boundary in not correctly modeled. The normal Reynolds stresses predicted by the CFD begin to depart from the DNS around $y^+ \approx 100$ and, approaching the wall, become isotropic by $y^+ \approx 0.5$ (see fig. 6b).

Figure 7 shows a comparison of the predicted turbulent kinetic energy budget with DNS. As a result of the damping of the linear terms in the expression for the Reynolds stresses (see eq. (47) and the location of the maximum and general profile of the production of turbulent kinetic energy, $\mathcal{P}_k$, the EASM fairly closely matches the

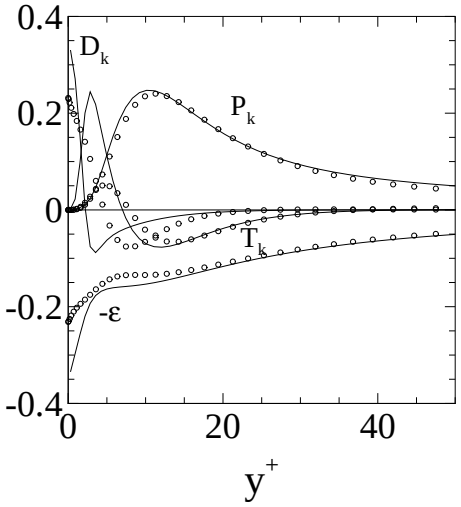

Figure 7: Comparisons with DNS at $R_\tau = 590$, turbulent kinetic energy budget. ——, EASM ; ○, DNS [Moser, Kim & Mansour].

DNS calculation. As a consequence the mean velocity profile is also well matched as seen in fig. 4a. The dissipation rate, ε, balances the viscous diffusion of k, $\mathcal{D}_k$, at the wall although the wall values of these two quantities are elevated. This is likely due to elevated near-wall asymptotic value of k (see fig. 5b).

The absence of a damping function in the turbulent eddy viscosity in the k and ε equations contributes to the excessively high level of the turbulent transport of k, T_k, compared to the DNS. Additionally it contributes to the T_k profile peak occurring too close to the wall (see EASM at $y^+ \approx 5$, fig. 7).

Zero pressure gradient flat plate

DNS data—Spalart[27] used a fully spectral method in space based on Fourier series in the directions parallel to the plate and an exponential mapping in the normal direction. The time integration uses a Runge-Kutta scheme for the transport terms and a Crank-Nicolson scheme for the viscous terms. The following section uses mean and turbulent flow data at the Reynolds number based on momentum thickness of 1410 from this DNS.

[27] P. Spalart. Direct Simulation of Turbulent Boundary Layers up to Re_θ = 1410. *J. Fluid Mech.*, 187:61–98, 1988.

Computational mesh for ISAAC—The 5-unit long, flat plate, single block grid had an H-type mesh topology. The computational domain included an inflow block extending 2.5 units upstream from the leading edge of the 5 unit flat plate. The initial streamwise grid spacing at the leading edge of the plate was 5.0×10^{-4} units and was exponentially stretched from the leading edge to the trailing edge at a rate of 4 percent with a total of 161 grid points. The first cell

height of the baseline grid was 1.0×10^{-6} units (first cell center at $y^+ \approx 0.1$) fixed at both ends of the plate and exponentially stretched from the surface to the outer boundary at a rate of 6 percent with a total of 201 grid points. The upper boundary was 5 units away. The baseline grid had the dimensions 201×201. Numerical transition to turbulent flow occurred around $R_x \approx 0.5 \times 10^6$ or $R_\theta \approx 500$, which corresponds to a physical distance of approximately 0.004 units downstream of the plate leading edge. Grid cell counts were divisible by eight to allow three levels of mesh sequencing and/or the use of a multigrid to assist solution convergence.

Grid density study—Figure 8 shows grid density effects for the zero pressure gradient flat plate. The solution functionals, local skin friction and boundary layer displacement thickness, are plotted against total cell count in fig. 8. These solution functionals are not monotonically grid converged at $R_\theta = 1410$, circle symbols in fig. 8a, because the skin friction of the 1/2 density solution is slightly higher than both the 1/8 density and baseline grid density solutions. The variations between the skin friction at $R_\theta = 1410$ for these 3 finest grids are within 1 percent. One sees a similar trend in the variation of the boundary layer displacement thickness at the same two stations, fig. 8b, where the 1/2 density grid solution produces results below those of both the 1/8 density and baseline density solutions. This is due to the point of transition from laminar to turbulent flow occurring further downstream for the 1/2 density grid than any other grid.

Further downstream of the turbulent transition point, the variation of local skin friction at $R_\theta = 1.0 \times 10^4$, square symbols in fig. 8a, did not change for the 3 finest grids. Variations in the turbulent transition point can be masked because the skin friction correlation (c_f vs. R_θ) use *local* functional values, that is, the local skin friction, $c_f = 2\tau_w/\rho u_\infty^2$, and a Reynolds number based on the local momentem thickness. Changes in the transition location globally affect the displacement thickness, hence the same non-monotonic grid density trend occurs at both R_θ stations, see square symbols in fig. 8b.

Figures 9 and 10 shows the variation in the solution with the grid density for the mean flow, turbulent kinetic energy, Reynolds shear stress at ($R_\theta = 1410$), the skin friction correlation and boundary layer thickness. The mean flow solution changed little with increase in grid resolution. Slightly more variance is observed in the turbulent kinetic energy and the turbulent shear stress at $y^+ \approx 200$ and above. This could be in part due to the differing states of transition of the boundary for each grid resolution solution.

The survey station of $R_\theta = 1410$ was only slightly downstream of the start of the numerical laminar-to-turbulent transition phenomena

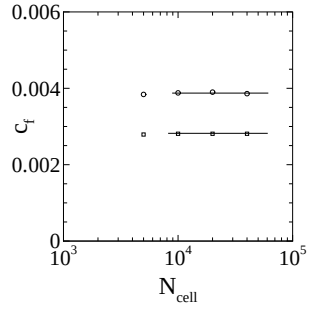

(a) c_f *vs.* total number of computational cells

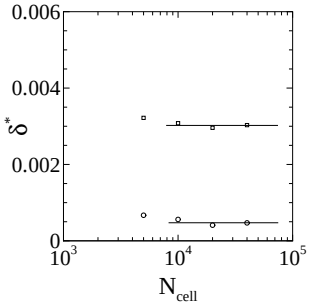

(b) δ^* *vs.* total number of computational cells

Figure 8: Effect of grid density on local skin friction and displacement thickness at fixed stations. ○, $R_\theta = 1410$. ; □, $R_\theta = 1.0 \times 10^4$; ——, Baseline grid reference line.

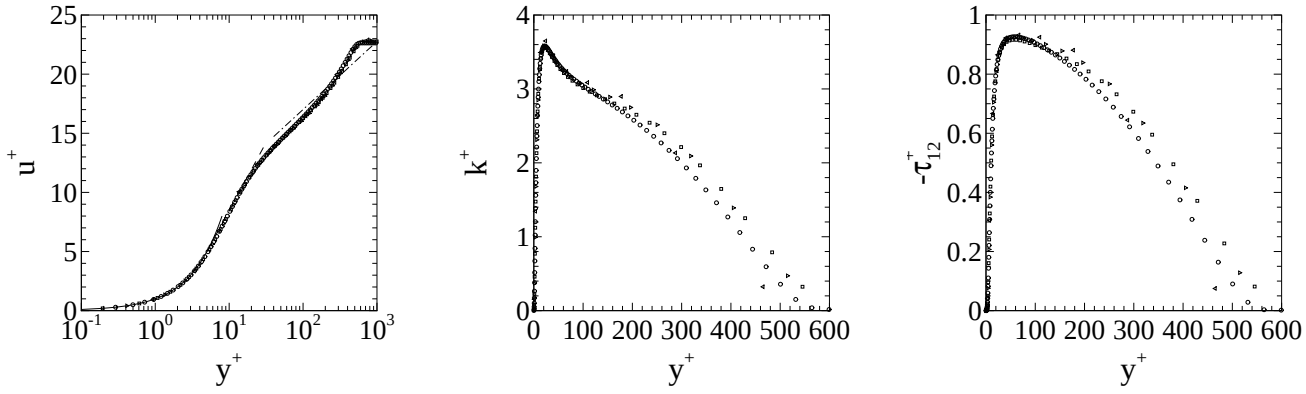

(a) Law-of-the-wall profiles (b) Turbulent kinetic energy (c) Turbulent shear stress

Figure 9: Effect of grid density at $R_\theta = 1410$. ○, Baseline grid ; □, 1/2 grid ; ▷, 1/4 grid ; ◁, 1/8 grid .

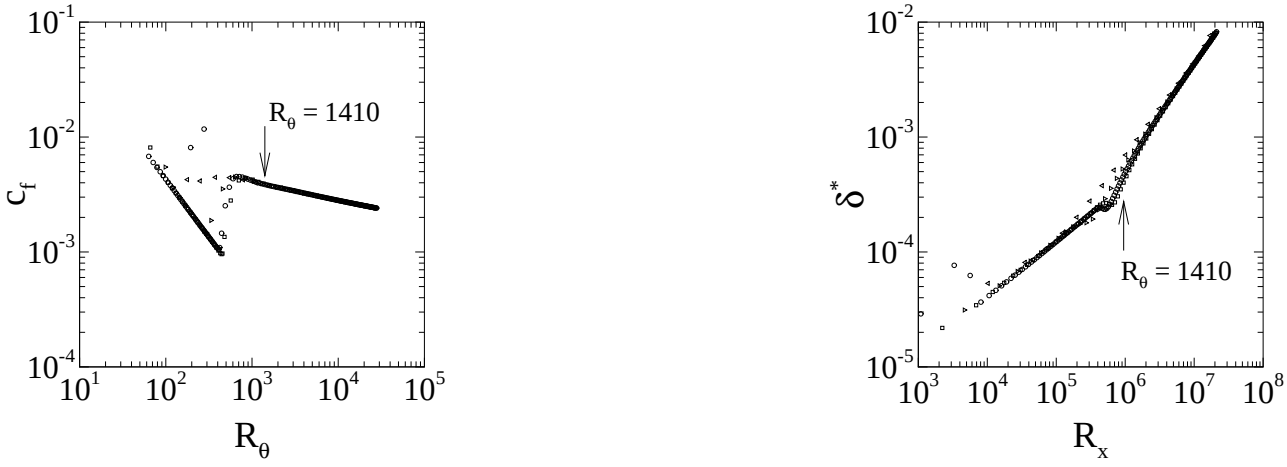

(a) Skin friction correlation (b) δ^* vs R_x

Figure 10: Effect of grid density at $R_\theta = 1410$. ○, Baseline grid ; □, 1/2 grid ; ▷, 1/4 grid ; ◁, 1/8 grid .

(constrast the location of $R_\theta = 590$ in figures 10a and 10b). Some distance appears to be required before 'fully' turbulent flow is achieved; therefore, in this transitional region the profiles of various quantities are subject to some distortion. The difference in the state of the boundary layer is not as apparent in fig. 10a as it is in fig. 10b, noting where $R_\theta = 1410$ falls in each plot, and that the variance in δ^* is observed. Appendix B briefly discusses various indicators of laminar or turbulent flow.

EASM comparisons with DNS—Figures 11 through 13 shows comparisons between the EASM and DNS for various quantities. Here as well, the EASM closely matched the DNS for the mean flow, turbulent kinetic energy, and the Reynolds shear stress. The general characteristics of the normal Reynolds stresses are captured similar to the channel flow, again with the exception of missing the nearwall anisotropy.

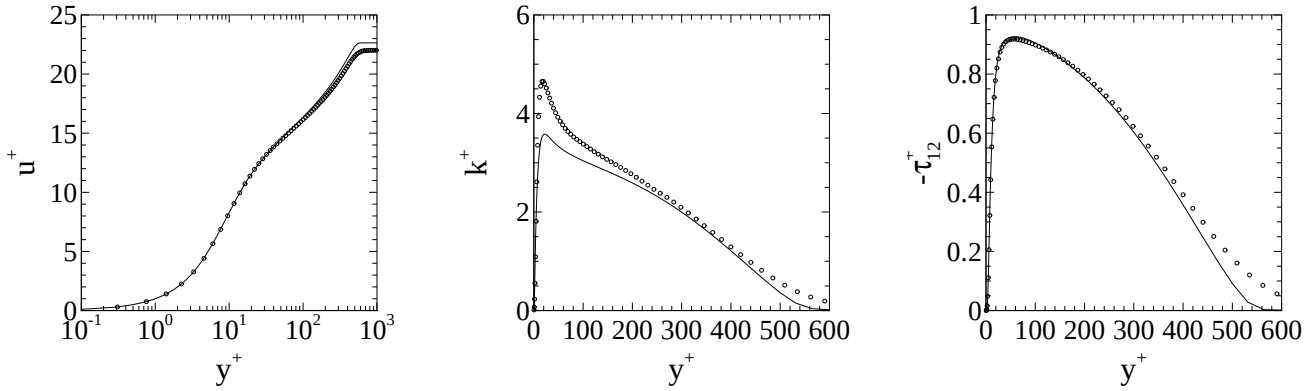

(a) Mean flow (log-linear scale) (b) Turbulent kinetic energy (linear scale) (c) Turbulent shear stress (linear scale)

Figure 11: A comparison of the mean velocity profiles with DNS at $R_\theta = 1410$. ——, EASM ; ○, DNS [Spalart]. .

The skin friction correlation, fig. 14a, has a distinct laminar characteristic followed by an apparently abrupt transition to turbulent like flow starting around $R_\theta = 400$. The growth of the displacement thickness, δ^*, displays a more gradual transition from the laminar to turbulent like flow spanning the Reynolds number range, $R_x \approx 4{\times}10^5$ to roughly 2.5×10^6, reference fig. 14b.[28] The trend and level of both the skin friction correlation and the growth of displacement thickness duplicate the classical theory well.

[28] $\delta^* = 1.728x/\sqrt{R_x}$ (Blasius) ; $\delta^* = 0.046x R_x^{-1/5}$ (turbulent); (F. M. White. *Viscous Fluid Flow*. McGraw-Hill, Inc., 1974)

Backward facing step

Experimental data—Driver *et al.*[29] obtained the data for this section from an experimental investigation that collected flow survey data for a rectangular channel with a backward facing step. The channel

[29] D. Driver and H. Seegmiller. Features of a Reattaching Turbulent Shear Layer in Divergent Channel Flow. *AIAA J.*, 23:163–171, 1985

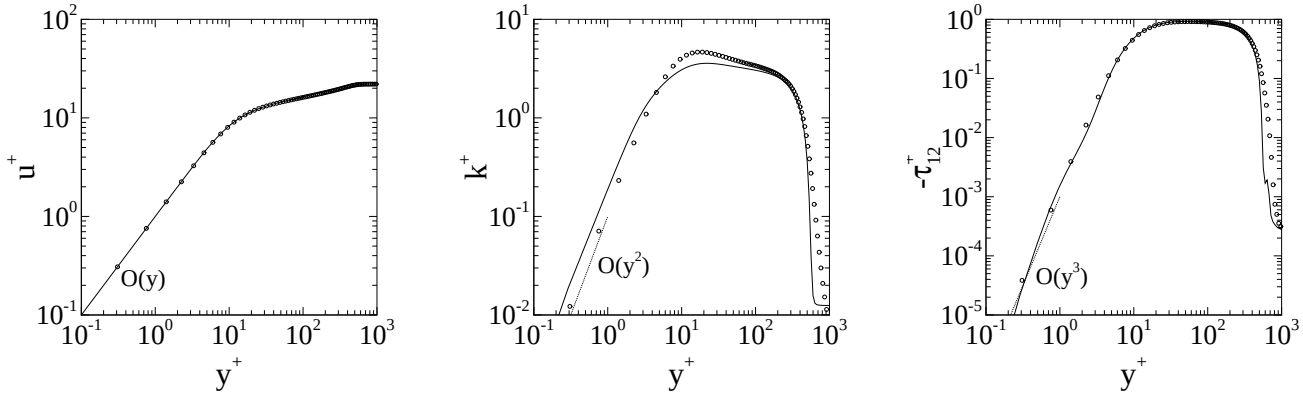

(a) Mean flow (log-linear scale) (b) Turbulent kinetic energy (log-log scale) (c) Turbulent shear stress (log-log scale)

Figure 12: A comparison of the mean velocity profiles with DNS at $R_\theta = 1410$. ——, EASM ; ○, DNS [Spalart]. .

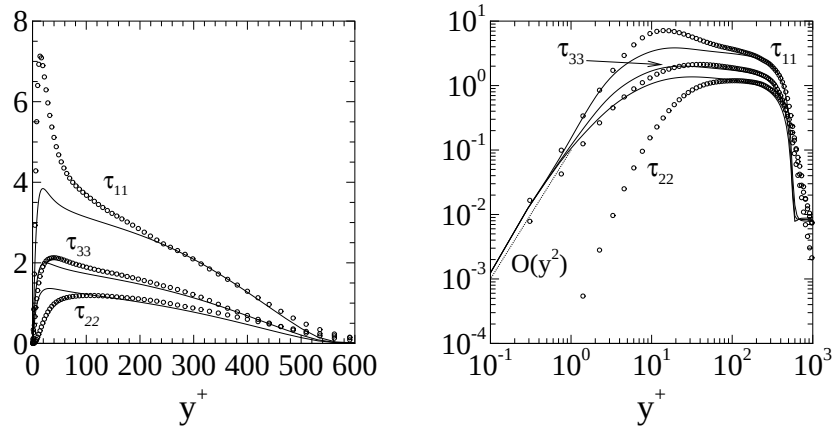

(a) Turbulent normal stresses (linear scale) (b) Turbulent normal stresses (log-log scale)

Figure 13: A comparison of the mean velocity profiles with DNS at $R_\theta = 1410$. ——, EASM ; ○, DNS [Spalart]. .

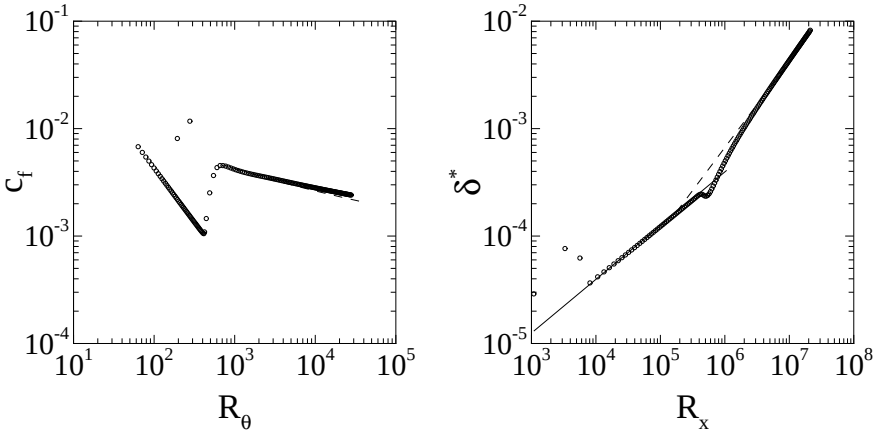

(a) Skin friction correlation

(b) δ^* *vs* R_x

Figure 14: Comparisons with classical theory. ○, EASM ;——, Blasius ; - - - -, turbulent.

consisted of a 1-m long, 10.1-cm high by 15.1-cm wide channel, followed by a 1.27-cm high step down. The top wall of the channel varied in angle from -2 degrees (inward) to 10 degrees (outward), creating either an adverse or positive pressure gradient downstream of the step. This study examines top wall angles of 0 and 6 degrees.

In units of the step height H, the upstream channel was 8 units high, followed by a constant channel height of 9 units for the 0 degree wall configuration. The channel height was 12.2 units for the 6 degree wall configuration at the outflow boundary 40 units downstream of the step face. In absolute units, the reference conditions were U_{ref} = 44.2 m/s, M_{ref} = 0.128, δ_{bl} = 1.9 cm, and R_θ = 5000 obtained from data at station x/H = -4.

Computational mesh for ISAAC—The computational domain consisted of two blocks; the upstream block modeled the region upstream of the backward facing step; and the downstream block included the step and region downstream of the step. The upstream and downstream blocks had the dimensions 121×113, and 201×225 respectively, with a 1:1 block interface. The cell height of the first cell was 1.0×10^{-6} m and was stretched away from the wall at the rate of approximately 15 percent until reaching the centerline of the channel. The streamwise grid spacing at the step wall was 5.0×10^{-4} m and was stretched away from that point at approximately 5 percent in the upstream and downstream directions.

The location of the inflow boundary was placed 1.0 m upstream of the step with subsonic conditions applied along that boundary. Turbulent flow developed "naturally" along the 1.0 m wall leading up to the location of the step. An alternative would be to define

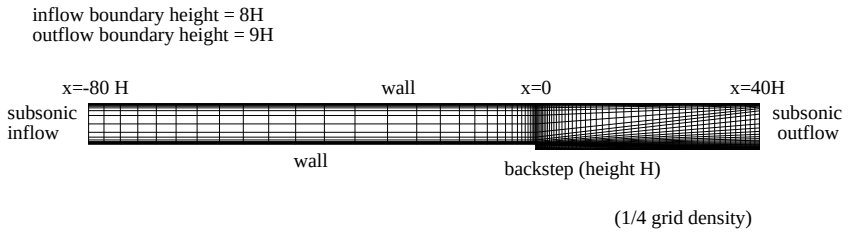

Figure 15: Backward facing step grid .

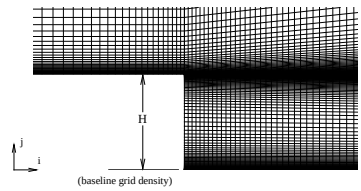

Figure 16: Detail of step for the backward facing step grid.

a set of fixed conditions at the reference station x/H = -4 derived from the specified experimental quantities. The backpressure along

Table 1: Flow Parameters for the Backward Facing Step

Case	$(p/p_\infty)_{outflow}$	M_{ref}	$\delta_{bl,ref}$(cm)	$R_{\theta,ref}$
Reference data		0.128	1.9	5000
EASM–$\alpha = 0$ deg.	1.00126	0.131	1.70	6160
EASM–$\alpha = 6$ deg.	1.0065	0.121	1.87	4750

the downstream outflow boundary was varied to approximate the stated conditions at the reference station of x/H = -4, see table 1. Figure 15 shows the entire computational domain and fig. 16 shows the detail of the gridding in the vicinity of the step.

Grid convergence—Figure 17 shows the variation of static pressure coefficient and local skin friction with grid density for the $\alpha = 0$ configuration. Similar solutions were calculated using the 1/4, 1/2, and baseline grids, the 1/8 density grid departing significantly from the other three grids.

Comparisons with experimental data—Figures 18 and 19 show comparisons of the experimental data with the ISAAC solutions using the EASM for both $\alpha = 0$ and $\alpha = 6$ degree configuration. The change in the static pressure coefficient with a variation in the wall angle is quite well captured though the actual levels are slightly elevated. The change in the local skin friction coefficient with the wall angle was similarly predicted though not quite matched as well. These results are similar to what has been published previously for the Rumsey-Gatski EASM for the $\alpha = 0$ configuration.[30] The earlier results predicted the shift in the boundary layer edge velocity with the wall angle, fig. 18c, though the absolute levels were low in the region downstream of the step probably due to a high back pressure. These results also predicted a change in the flow reattachment point with the wall angle though the level was shifted upstream of the

[30] C. Rumsey and T. Gatski. Summary of EASM Turbulence Models in CFL3D With Validation Test Cases. NASA TM–2003-212431, June 2003.

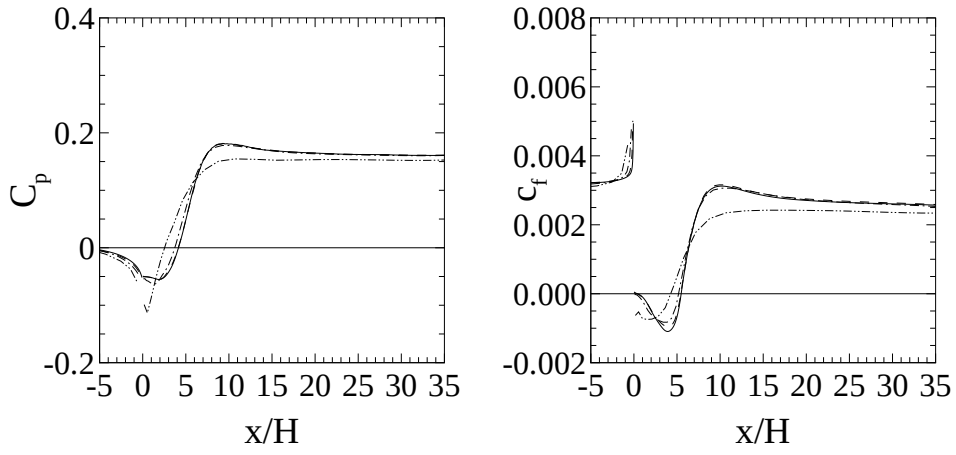

(a) Static pressure coefficient (b) Local skin friction coefficient

Figure 17: Variation with grid density, backward facing step, $\alpha = 0$. ——, Baseline grid ; ----, 1/2 grid ; $- \cdot -$, 1/4 grid ; $- \cdot \cdot -$, 1/8 grid.

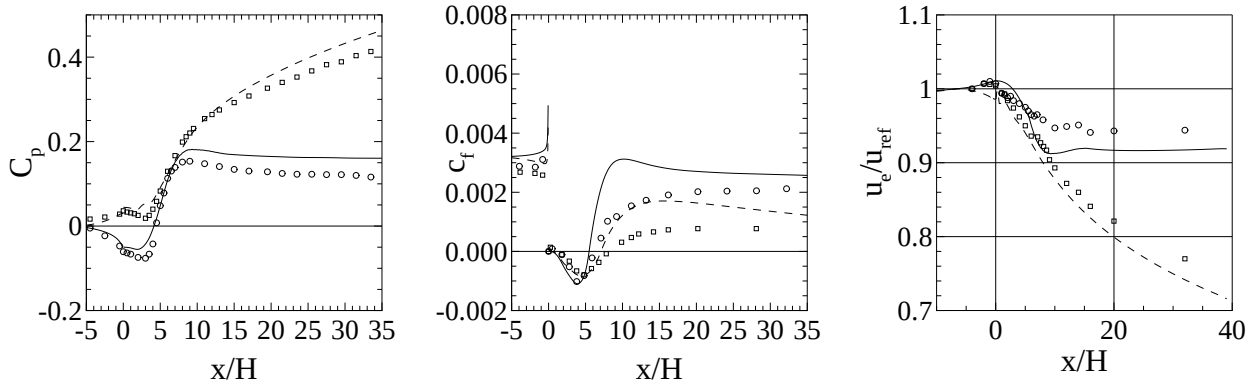

(a) Static pressure coefficient (b) Local skin friction coefficient (c) Normalized boundary layer edge velocity

Figure 18: Variation with wall divergence angle, backward facing step. ○, Data, $\alpha = 0$; □, Data, $\alpha = 6$ [Driver and Seegmiller] ; ——, EASM, $\alpha = 0$; ----, EASM, $\alpha = 6$.

data, fig. 19. The error bar on the experimental data is from the published uncertainty in the determination of the point of flow reattachment. The error bar applied to the CFD data was the local grid spacing. The local grid spacing was considered to be the finest resolution possible for determining the reattachment point.

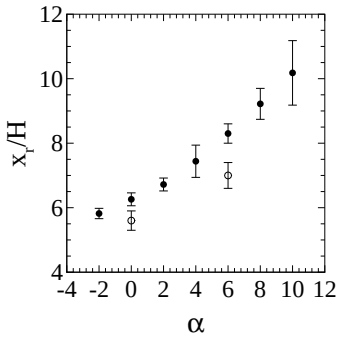

Figure 19: Variation of reattachment point with wall angle, backward facing step. •, Data [Driver and Seegmiller] (Error bar indicates stated experimental uncertainty) ; ○, EASM (Error bar indicates local grid spacing) .

Axisymmetric afterbody

Test facility—This test case was an axisymmetric geometry that was part of a series of models tested in both the Langley 1/3-m Pilot Transonic Cryogenic Tunnel, fig. 20, and the Langley 16-Foot Transonic Tunnel. The Pilot Tunnel had an octagonal test section with slots at the corners of the octagon similar to the Langley 16-Foot Transonic Tunnel test section.[31] The test medium for the cryogenic

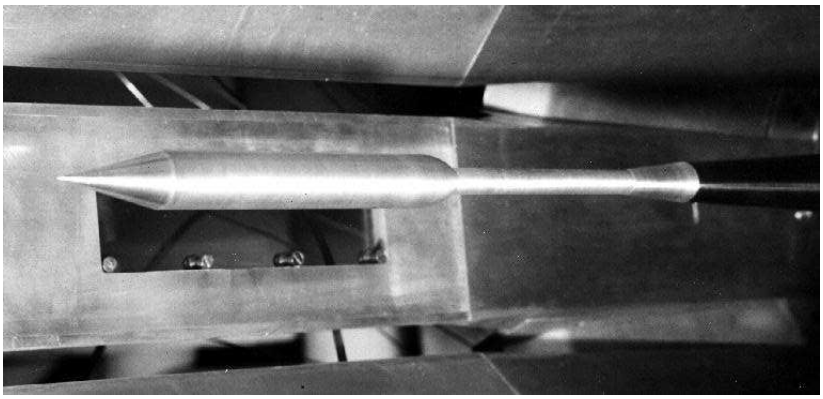

Figure 20: Axisymmetric afterbody model in 1/3-meter Pilot Transonic Cryogenic Tunnel .

tunnel was liquid nitrogen cooled air. High Reynolds number data were obtained in the Pilot Tunnel through a combination of cryogenic freestream temperatures and freestream total pressure that were independently controllable. Approximately 5 atm of pressure and 100K total temperature produced a unit Reynolds number of 260×10^6/m.

This test case conducted the experiment over a range of temperatures from approximately 100K to 300K and pressures from 1 to 5 times the standard atmospheric level. Several variations of freestream total temperatures or pressures resulted in the same free stream Reynolds number. Surface pressure coefficients and nozzle-boattail drag were shown to be similar, regardless of the temperature and pressure combinations that created the equivalent Reynolds numbers.

Previously[32] high Reynolds number simulations with a CFD solver were obtained through increased total pressure alone rather than through a combination of freestream total pressure and using

[31] R. Kilgore, J. Adcock, and J. Edward. Flight Simulation Characteristics of the Langley High Reynolds Number Cryogenic Transonic Tunnel. AIAA Paper 74-80, January 1974.

[32] J.-R. Carlson. Prediction of High Reynolds Number Flow Using Algebraic Reynolds Stress Turbulence Models, Part 2: Transonic Shock-Separated Afterbody. *J. Propulsion and Power*, 13:620–628, 1997.

cryogenic temperatures. The temperature range of Sutherland's law used for calculating bulk viscosity imposes some limits to the input flow conditions. ISAAC input parameters are Reynolds number per unit grid length, static temperature and Mach number, so similarly, the high Reynolds number conditions were obtained through a change in density rather than cyrogenic temperatures.

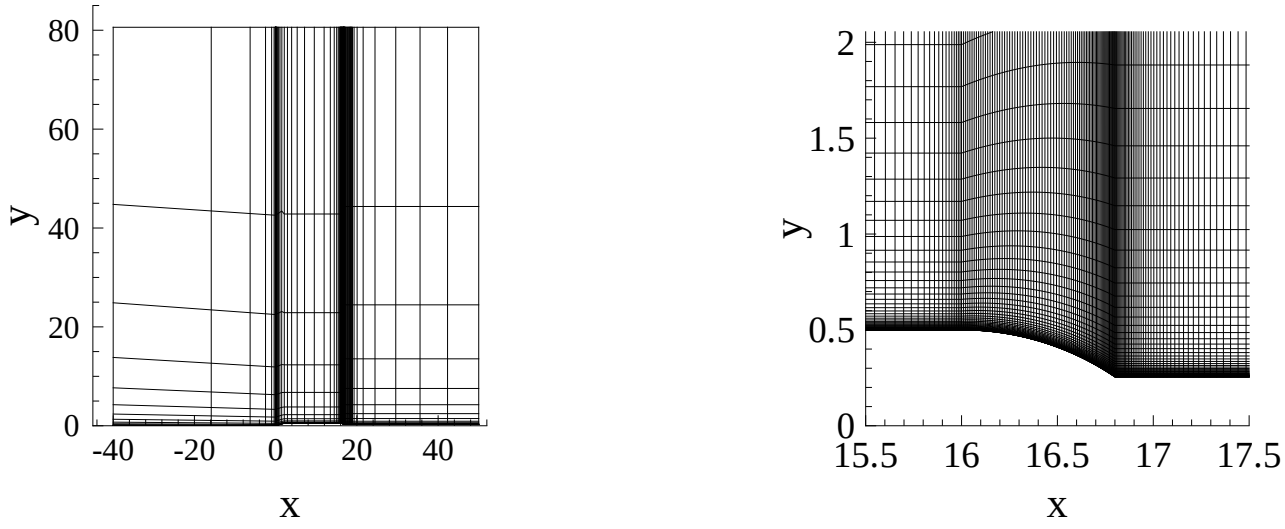

(a) 1/4 grid.

(b) Detail of afterbody region-baseline grid

Figure 21: Axisymmetric afterbody computational grid

Axisymmetric Afterbody Model and Conditions—The model validation geometry presented herein is one of six models that were built for a Reynolds number investigation performed by Reubush.[33] This model had a characteristic length of 16 in. and the boattail geometry was a circular-arc, with a length-to-maximum-diameter ratio (fineness ratio) of 0.8 boattail. The nose of the model was a 28° cone, 1.7956 in. long, fairing to the cylindrical body via a 1.3615-in.-radius circular-arc whose center is 2.125 in. downstream of the model nose and 0.8615 in. below the model centerline.

The circular-arc fairing is tangent at its endpoints to the conical nose (1.7956 in. from the nose) and cylindrical body (2.125 in. from the nose). The model was sting mounted with the diameter of the sting being equal to the model base diameter. The length of the constant diameter portion of the sting (6.70 in. measured from the nozzle connect station) was such that there should be no effect of the sting flare downstream of the nozzle trailing edge on the boattail pressure distributions. These numbers will produce an analytically consistent surface definition. The model was cast aluminum and from conversations with the original test enginer, it was felt that the models were possibly not manufactured to tolerances that would

[33] D. Reubush. The Effect of Reynolds number on Boattail Drag. AIAA paper 75-63, January 1975; D. Reubush and L. Putnam. An Experimental and Analytical Investigation of the Effect on Isolated Boattail Drag of Varying Reynolds Number up to 130×10^6. NASA TND–8210, May 1976; and D. Reubush. Experimental Investigation to Validate Use of Cryogenic Temperatures to Achieve High Reynolds Numbers in Boattail Pressure Testing. NASA TM X–3396, August 1976 .

have produced an analytically smooth shape.

The grid utilizes an H-type mesh topology, see fig. 21. The block dimensions are divisible by 4 to facilitate investigating grid density effects on the flow solution. The mesh is gridded with the streamwise flow direction oriented along the i index and the j index in the normal direction. The body is described using 100 cells extending from the leading edge of the nose to the nozzle connect station and 80 cells from the nozzle connect station to the nozzle-boattail trailing edge, as well as, 80 cells extending 80 body radii from the body surface to the far field. The boundary layer grid expansion rate away from the body is approximately 16 percent. The inflow boundary is 40 body radii upstream of the model nose and the outflow boundary is 35 radii downstream of the nozzle boattail. Solid walls are treated as no-slip adiabatic surfaces. Riemann invarinats along characteristics are specified for boundary conditions along the inflow and the lateral freestream outer boundaries of the flow domain. The extrapolation boundary condition is applied on the downstream outflow face. The flux limiter is min-mod and mesh sequencing is used to enhance numerical convergence of the solution.

Table 2: Schedule of Reynolds Number and Grid Spacing Normal to the Wall

R($\times 10^6$)	R($\times 10^6$)/in.	h_1 (in.)
7.0	0.4375	6×10^{-5}
128.3	8.0313	2×10^{-6}

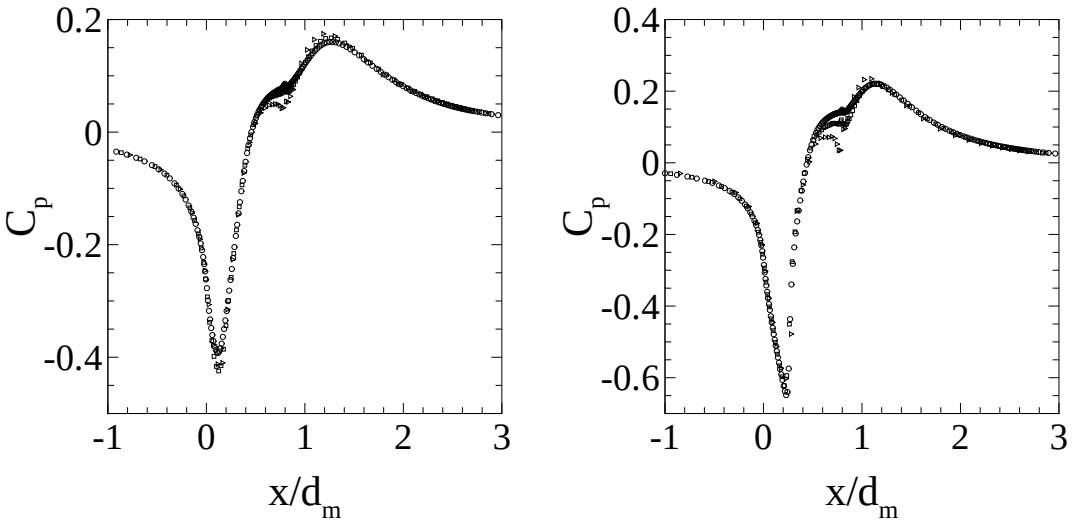

(a) R = 7×10^6 (b) R = 128.5×10^6

Figure 22: Variation of afterbody pressure coefficient with grid density, M = 0.9, L = 16. ○, baseline grid; □, 1/2 grid, ▷, 1/4 grid .

The freestream conditions for the axisymmetric CFD cases were M = 0.9, $T_\infty = 300$F, using air at $\gamma = 1.4$. The first cell height of the grid of each configuration was different for each freestream Reynolds number according to table 2. Input Reynolds numbers of 4.375×10^5/in. and 8.0313×10^6/in. were used to develop the low and high Reynolds number solutions respectively.

Figure 22 shows grid sensitivity of the EASM at M = 0.9 at the lowest and highest Reynolds number for this test case, (a) R = 7×10^6 and (b) R = 128×10^6 respectively. These sensitivities were relatively consistent for the other turbulence models and other viscous models investigated.[34] The EASM prediction of the afterbody shock strength and pressure recovery was Reynolds number dependent, see fig. 23.

[34] J.-R. Carlson. Prediction of High Reynolds Number Flow Using Algebraic Reynolds Stress Turbulence Models, Part 2: Transonic Shock-Separated Afterbody. *J. Propulsion and Power*, 13:620–628, 1997.

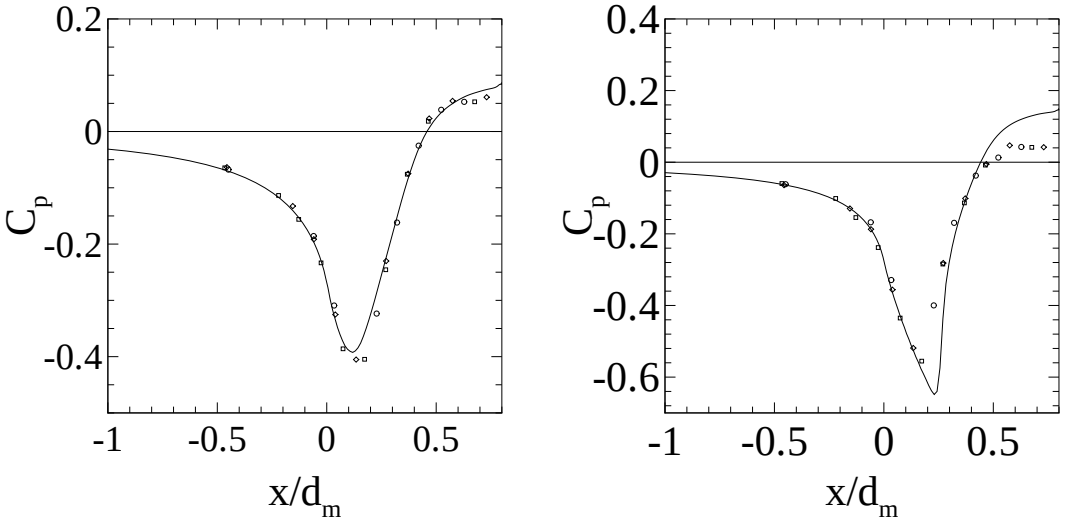

(a) R = 7×10^6 (b) R = 128.5×10^6

Figure 23: Comparison of afterbody pressure coefficients with experimental data at M = 0.9, L = 16. ——, EASM ; ○, $\phi = 0$; □, $\phi = 120$; ◇, $\phi = 240$ Data [Reubush] .

N–Version Testing

Flat plate

Figures 24 through 30 compare the solutions produced by the ISAAC code with those produced by the PAB3D code for the zero pressure gradient flat plate. Several flow variables, such as mean flow and turbulence quantities, are compared at two stations, R_θ = 1410 and $R_\theta \approx 10000$, followed by comparisons of the development of boundary layer displacement thickness, shape factor and the skin friction correlation.

A very good match has been obtained between the two solvers for the mean flow at station R_θ = 1410, see fig. 24, but the turbulent kinetic energy and Reynolds shear stress at station R_θ = 1410 are not as close, see figs. 25 , 26 and 27. Further downstream of the numerical transients caused by the transition to turbulent flow at the station $R_\theta \approx$10000, the two codes appear to match more closely, see figs. 28 and 29.

The first boundary layer shape factor, H_{12} and the skin friction

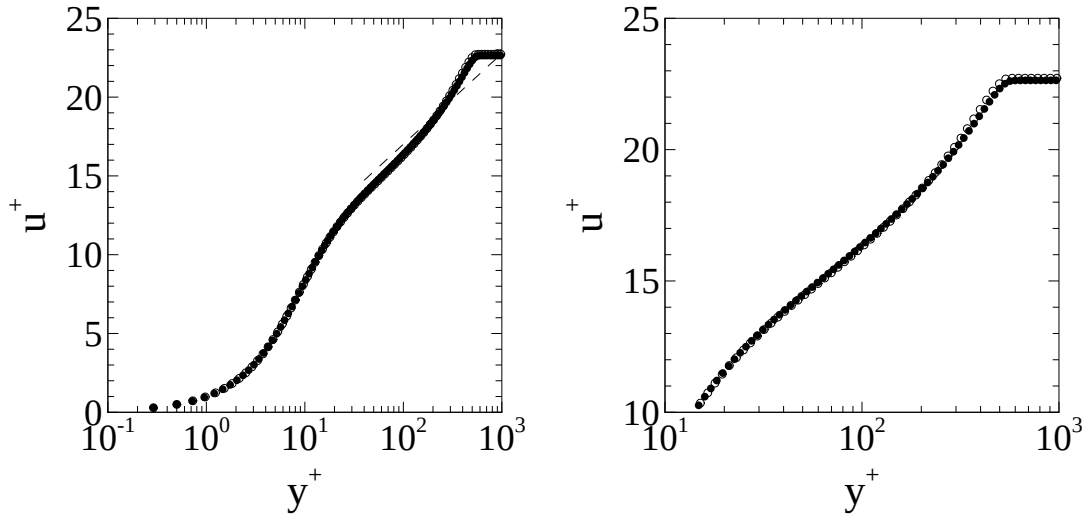

(a) Mean flow, Log-linear scale

(b) Mean flow, Detail of log-layer

Figure 24: Zero pressure gradient flat plate at $R_\theta = 1410$. •, ISAAC; ○, PAB3D .

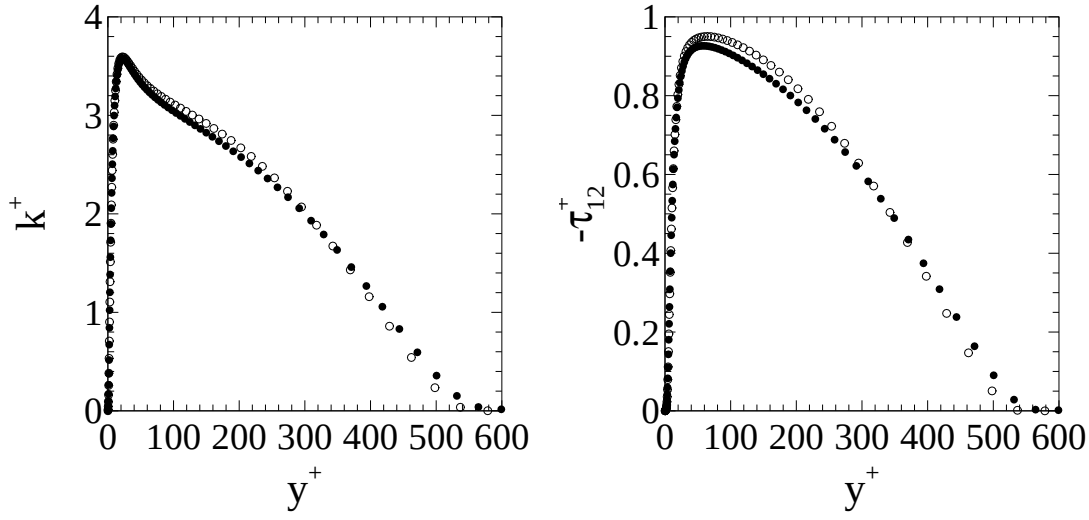

(a) Turbulent kinetic energy.

(b) Reynolds shear stress.

Figure 25: Zero pressure gradient flat plate at $R_\theta = 1410$, linear scale. •, ISAAC; ○, PAB3D .

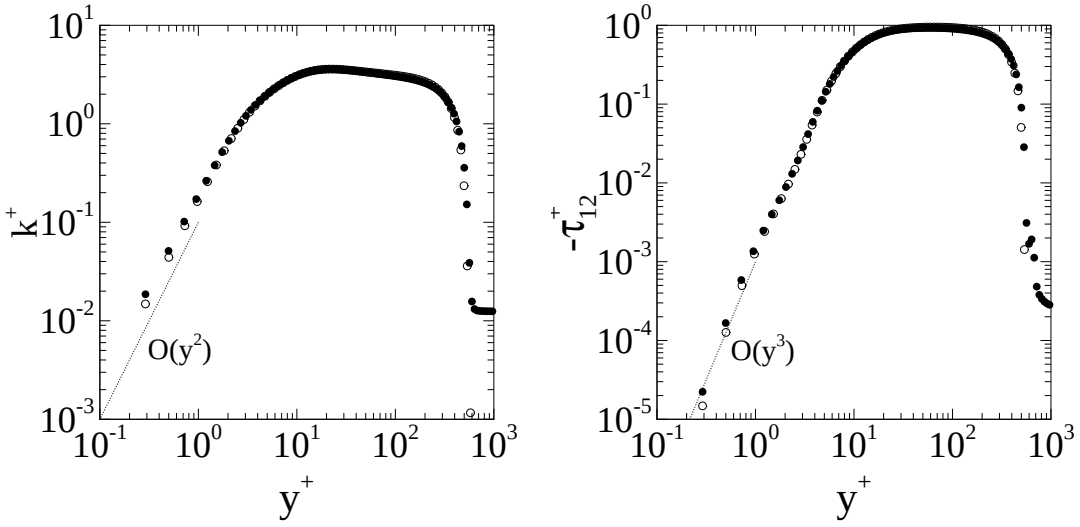

(a) Turbulent kinetic energy.

(b) Reynolds shear stress.

Figure 26: Zero pressure gradient flat plate at $R_\theta = 1410$, log-log scale. •, ISAAC; ○, PAB3D .

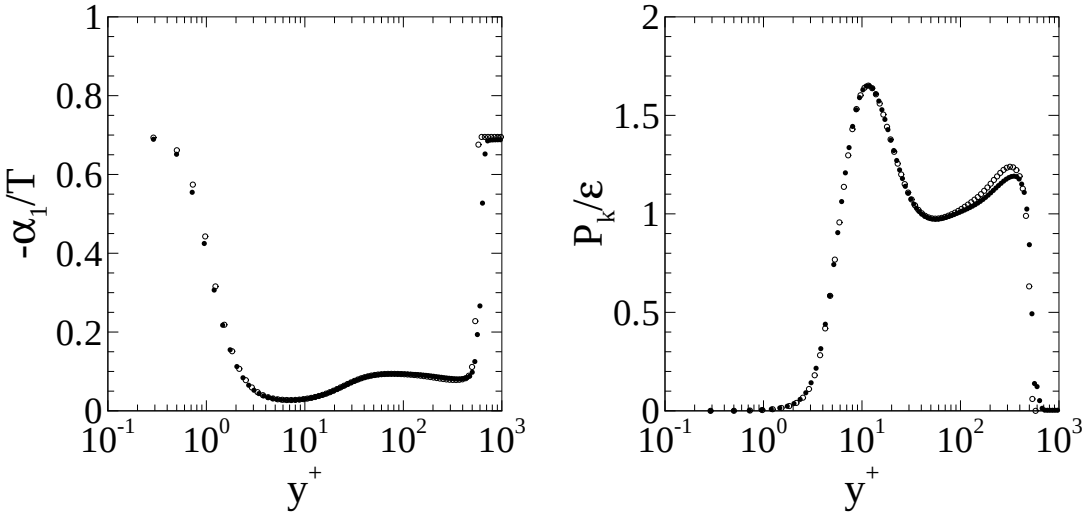

(a) $-\alpha_1/\mathrm{T}$

(b) P_k/ε.

Figure 27: Zero pressure gradient flat plate at $R_\theta = 1410$. •, ISAAC; ○, PAB3D .

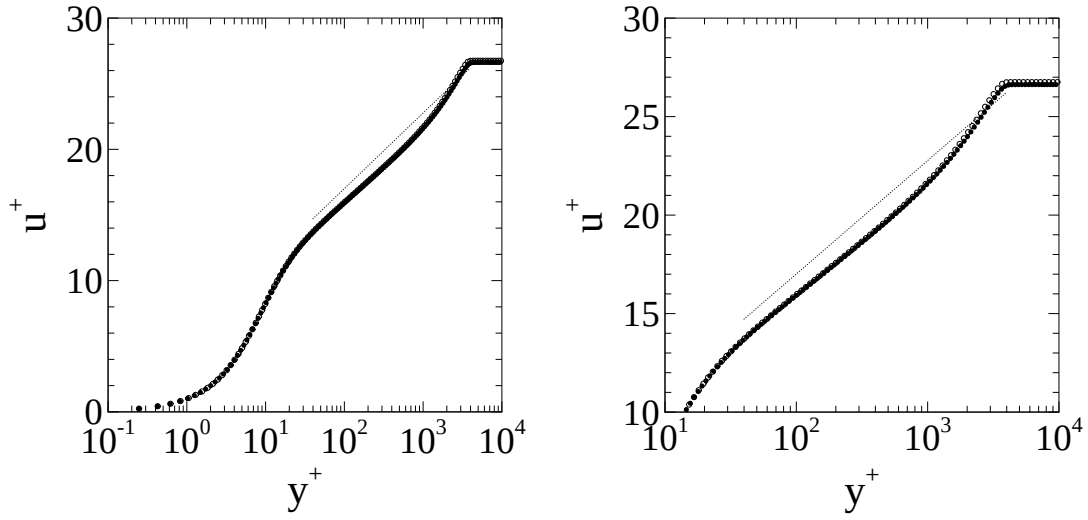

(a) Log-linear scale.

(b) Detail of log-layer.

Figure 28: Zero pressure gradient flat plate at $R_\theta = 10^4$, mean flow. •, ISAAC; ○, PAB3D ; $\cdots$, log-layer.

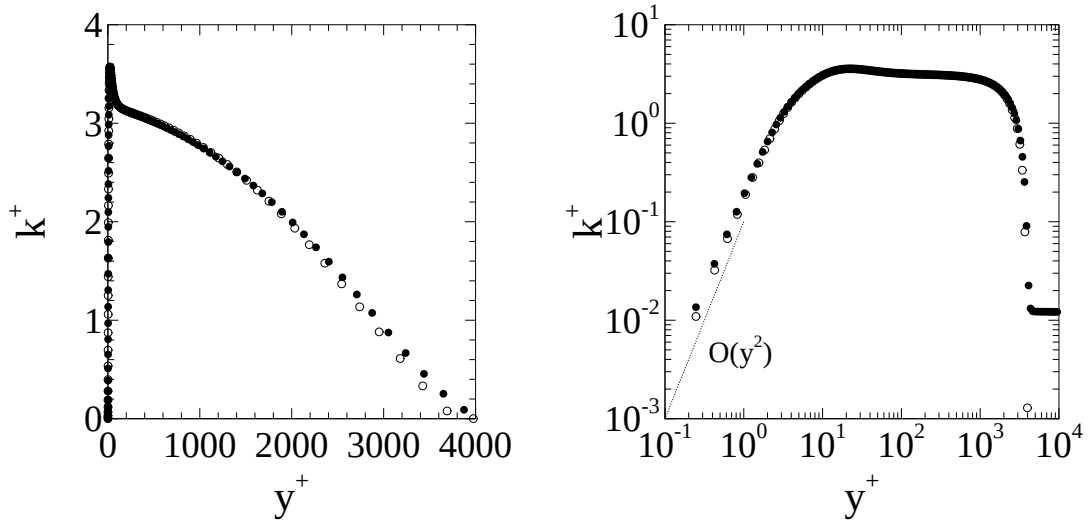

(a) Linear scale

(b) Log-log scale

Figure 29: Zero pressure gradient flat plate at $R_\theta = 10^4$, turbulent kinetic energy. •, ISAAC; ○, PAB3D ; $\cdots$, log-layer.

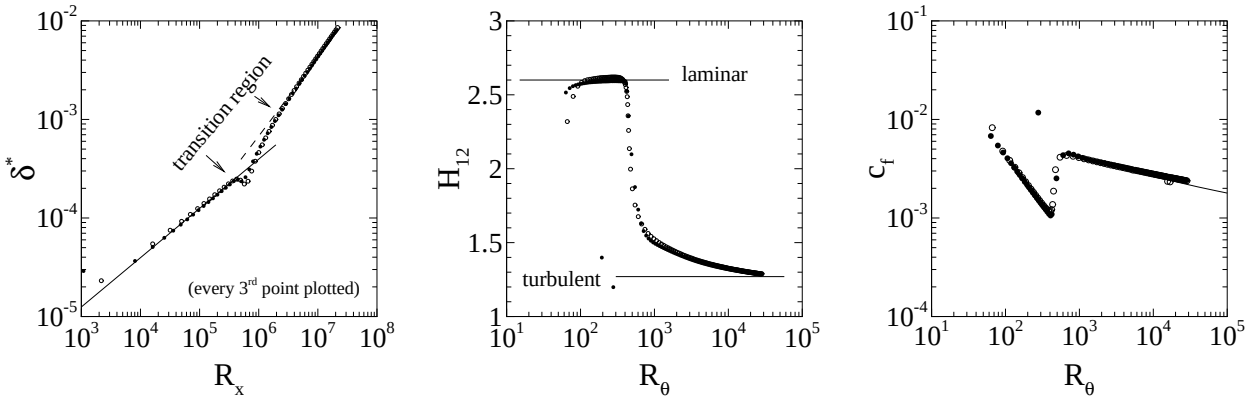

(a) Momentum thickness with local Reynolds number

(b) First shape factor

(c) Skin friction correlation

Figure 30: Zero pressure gradient flat plate. •, ISAAC; ○, PAB3D ; ——, Linear theory-laminar ; ----, Linear theory-turbulent.

correlation, c_f *vs* R_θ, are also quite closely matched with only minor variances seen in the upstream laminar portion of the flat plate, see figs. 30b and 30c. Similarly, the development of the the displacement thickness with Reynolds number, fig. 30a, for the most part is identical between ISAAC and PAB3D. A slight departure occurs in the the laminar-to-turbulent transition region, $3 \times 10^5 < R_x < 2 \times 10^6$, but is relatively local and does not appear to affect the downstream match significantly.

Axisymmetric afterbody

Using the two codes, fig. 31 compares the static pressure coefficients on the afterbody. A slightly higher pressure occurs in the ISAAC solution compared with the PAB3D solution for the lower Reynolds number case, see fig. 31a just downstream of $x/d_m = 0.0$. The high Reynolds number comparison show virtually identical static pressure distributions on this portion of the model.

Initially, the solutions developed using ISAAC had a considerably weaker shock because of the type of limiter being applied to the inviscid fluxes. Since the PAB3D solutions were developed using the min-mod limiter, changing the limiter being used in the ISAAC calculations from Venkatakrishnan's smoothing limiter to the min-mod resolved this difference in the solutions between the two solvers.

4 Summary

The turbulence equations being solved in the three-dimensional Reynolds averaged Navier-Stokes (RANS) code PAB3D have

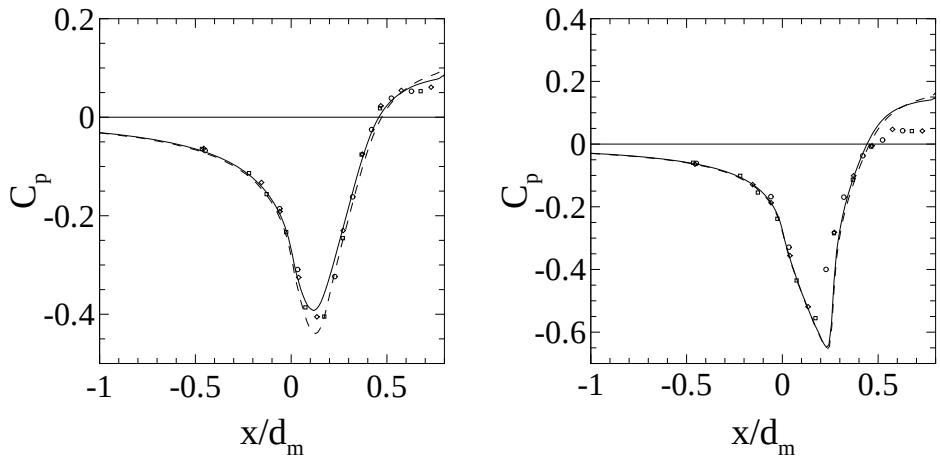

(a) R = 7.0×10^6 (b) R = 128.5×10^6

Figure 31: Comparison of static pressure coefficients, axisymmetric afterbody, M = 0.9, L = 16. ——, ISAAC ; - - - -, PAB3D ; ○, $\phi = 0$; □, $\phi = 120$; ◇, $\phi = 240$, Data [Reubush].

been implemented in the three-dimensional RANS code ISAAC. Initial validation of the implementation was accomplished through comparisons with data for four test cases: channel flow, zero pressure gradient flat plate, backward facing step and an axisymmetric transonic afterbody flow. These test cases covered a wide range of fluid dynamic situations, including compressible flow, separated flow, and high Reynolds number flow. The turbulence equations were able to simulate all of these flow situations fairly well. Additionally, excellent agreement was achieved in comparisons between solutions developed using ISAAC and with solutions developed using the solver PAB3D.

A Nomenclature

Symbol	Definition
$\mathbf{b}$, b_{ij}	Reynolds stress anisotropy tensor
C_μ^*	Variable model coefficient, $-\alpha_1/T$
C_p	Pressure coefficient, (p - p_∞) / q_∞
c_f	Local skin friction coefficient, τ_w / q_∞
d_m	Body maximum diameter (1.0 in.) [axisymmetric afterbody]
H	Backward facing step height
H_{12}	First boundary layer shape factor, (δ^*/θ)
h, δ_h	Channel half-height
h_1	Physical height of first computational grid from a wall
L	Reference length [axisymmetric afterbody]
M	Mach number
N_{cell}	Total number of computational cells
$\boldsymbol{\mathcal{P}}$	Production, $-\tau_{ik}(\partial u_j/\partial x_k) - \tau_{jk}(\partial u_i/\partial x_k)$
$\mathcal{P}_k$	Production of turbulent kinetic energy, $-\frac{1}{2}\{\boldsymbol{\mathcal{P}}\} = \tau_{ij}\,(\partial u_i/\partial x_j)$
p	Static pressure
q	Dynamic pressure
R	Reynolds number based on model reference length, ($u_\infty L/\nu$)
R_t	Cell turbulent Reynolds number, $k^2/(\nu\varepsilon)$
R_x	Reynolds number based on distance x, ($u_\infty x/\nu$)
R_θ	Reynolds number based on momentum thickness, ($u_\infty\theta/\nu$)
R_τ	Reynolds number based on wall shear stress, ($u_\tau h/\nu$)
$\mathbf{S}$, S_{ij}	Symmetric velocity gradient tensor, $(\partial u_i/\partial x_j + \partial u_j/\partial x_i)\,/2$
T	Kinematic time scale, k/ε
$\mathbf{u}$, u_i	Velocity vector
u^+	Law-of-the-wall coordinate, u/u_τ
u_τ	Local friction velocity, $\sqrt{\tau_w/\overline{\rho}_w}$
$\mathbf{W}$, W_{ij}	Antisymmetric velocity gradient tensor, $(\partial u_i/\partial x_j - \partial u_j/\partial x_i)\,/2$
x	Streamwise distance
$\mathbf{x}$, x_i	Position vector
x_r	Point of flow reattachment
y	Vertical distance
y^+	Law-of-the-wall coordinate, y u_τ / ν
α	Wall divergence angle (backward facing step)
α_n	scalar coefficient
δ	Boundary-layer thickness, value of y at 0.995 u_{max}
δ^*	Displacement thickness, $\int_0^\delta$(1-u/u_e)dy
η_1^*	Flow invariant, $T^2\{\mathbf{S}^2\}$
η_2^*	Flow invariant, $T^2\{\mathbf{W}^2\}$
θ	Momentum thickness, $\int_0^\delta$ (u/u_e) (1 - u/u_e) dy
$\overline{\mu}$	Laminar viscosity
μ_t	Turbulent eddy viscosity, $C_{\mu_0}\overline{\rho}k^2/\varepsilon$
ν	Kinematic viscosity, μ / $\overline{\rho}$
$\overline{\rho}$	Density
$\boldsymbol{\tau}$, τ_{ij}	Reynolds stress tensor
τ_w	Shear stress at the wall, $\overline{\rho}_w$ du/dn
ϕ	Angular location of pressure orifices, deg. (axisymmetric afterbody)
bl	Boundary layer
ref	Reference conditions
w	Condition at wall surface
∞	Freestream condition

B A Comparison of Transition Indicators

There are several parameters that can indicate the presence of turbulent flow, or as the case may be, *developing* turbulent flow over the flat plate. These indicators occur both at a primative level, *e.g.*, peak turbulent kinetic energy and dissipation rate level at the wall; or at a derived level, *e.g.*, local skin friction, the rate of boundary layer growth with local Reynolds number, or boundary layer shape factors, to name a few examples.

Typically, a variation of the local skin friction with the local Reynolds number, fig. 32 is plotted, which clearly deliniates the change from laminar flow by the rather abrupt discontinuity in the curve around $R_x = 400{,}000$.

If the Reynolds number based on the momentum thickness of the boundary layer is used instead of the local Reynolds number, an equally abrupt change in the skin friction correlation from laminar flow to turbulent flow levls is observed, fig. 33. At first glance, the local skin friction in these two figures appears to attain a fully turbulent level almost immediately downstream of the transition point. (As noted on the figure, the momentum Reynolds number of 410 is approximately coincident with the local Reynolds number of 400,000 and is used as a reference point for the discussion.)

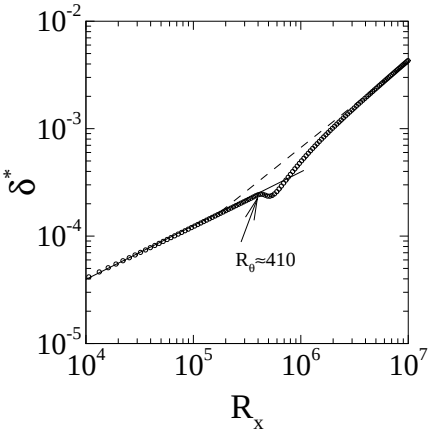

Figure 34: Displacement thickness with local Reynolds number (detail). ○, EASM ;——, Blasius ;----, turbulent (flat plate theory) .

A slightly different conclusion could be drawn (concerning the transition of the flow from laminar to turbulent flow) from a plot of the rate of growth in the boundary layer displacement thickness with local Reynolds number, fig. 34. The displacement thickness only gradually approaches the turbulent level as the Reynolds number increases downstream of the transition point marked ($R_\theta \approx 410$).[35]

Similarly the first shape factor, $H_{12} = \delta^*/\theta$, shows a clear departure from laminar flow, fig. 35, but a rather prolonged region

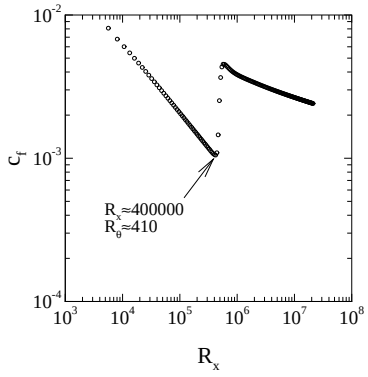

Figure 32: Local skin friction with local Reynolds number. ○, EASM.

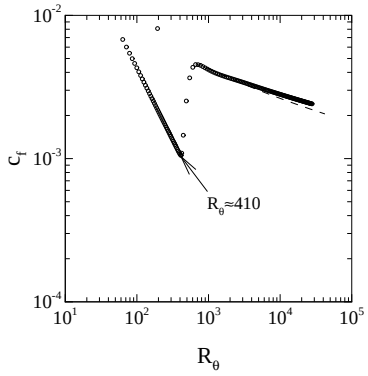

Figure 33: Skin friction correlation. ○, EASM ;----, Karman-Shoenherr empirical curve.

[35] M. Rai and P. Moin. Direct Numerical Simulation of Transition and Turbulence in a Spatially Evolving Boundary Layer. *Journal of Computational Physics*, 109:169–192, 1993.

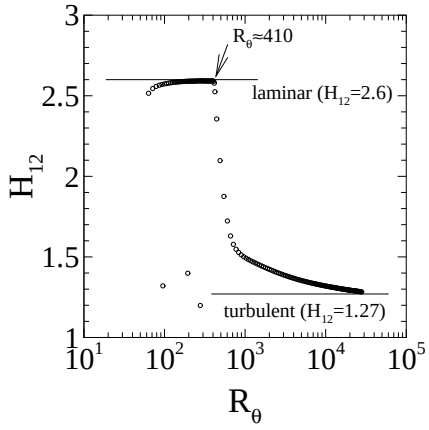

Figure 35: First shape factor with momentum thickness Reynolds number. ○, EASM .

of developing turbulent flow before the shape factor approaches the classically derived level.

If the "simpler" parameter of peak turbulent kinetic energy is plotted against Reynolds number, a less definitive picture appears as to the point of transition, fig. 36. For reference, the figures show the locations of $\mathrm{R}_x \approx 400000$ and $\mathrm{R}_\theta \approx 410$.

Though still somewhat abrupt at transition, the peak turbulent kinetic energy has a region of gradual increase in intensity before increasing another two orders of magnitude greater than the level in the region of laminar flow, in the current example, starting from a value around 10^{-6}.

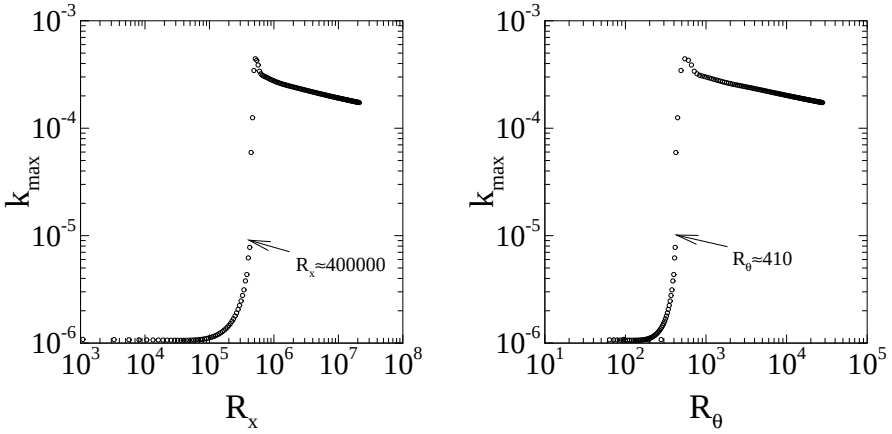

(a) k_{peak} *vs.* R_x. (b) k_{peak} *vs.* R_θ.

Figure 36: Streamwise variation of peak turbulent kinetic energy.

REPORT DOCUMENTATION PAGE	Form Approved OMB No. 0704–0188

1. REPORT DATE *(DD-MM-YYYY)*	2. REPORT TYPE	3. DATES COVERED *(From - To)*
01-12-2005	Technical Memorandum	

4. TITLE AND SUBTITLE
Assessment of an Explicit Algebraic Reynolds Stress Model

5a. CONTRACT NUMBER

5b. GRANT NUMBER

5c. PROGRAM ELEMENT NUMBER
26-065-30-35

6. AUTHOR(S)
Carlson, Jan-Reneé

5d. PROJECT NUMBER

5e. TASK NUMBER

5f. WORK UNIT NUMBER
23-065-30-35

7. PERFORMING ORGANIZATION NAME(S) AND ADDRESS(ES)
NASA Langley Research Center
Hampton, VA 23681-2199

8. PERFORMING ORGANIZATION REPORT NUMBER
L–19103

9. SPONSORING/MONITORING AGENCY NAME(S) AND ADDRESS(ES)
National Aeronautics and Space Administration
Washington, DC 20546-0001

10. SPONSOR/MONITOR'S ACRONYM(S)
NASA

11. SPONSOR/MONITOR'S REPORT NUMBER(S)
NASA/TM–2005–213771

12. DISTRIBUTION/AVAILABILITY STATEMENT
Unclassified-Unlimited
Subject Category 01
Availability: NASA CASI (301) 621-0390

13. SUPPLEMENTARY NOTES
An electronic version can be found at http://ntrs.nasa.gov

14. ABSTRACT

This study assesses an explicit algebraic Reynolds stress turbulence model in the in the three-dimensional Reynolds averaged Navier-Stokes (RANS) solver, ISAAC (Integrated Solution Algorithm for Arbitrary Con gurations). Additionally, it compares solutions for two select con gurations between ISAAC and the RANS solver PAB3D. This study compares with either direct numerical simulation data, experimental data, or empirical models for several di erent geometries with compressible, separated, and high Reynolds number ows. In general, the turbulence model matched data or followed experimental trends well, and for the selected con gurations, the computational results of ISAAC closely matched those of PAB3D using the same turbulence model.

15. SUBJECT TERMS
CFD, turbulence modeling, code assessment, Reynolds stress, explicit algebraic stress model

16. SECURITY CLASSIFICATION OF:			17. LIMITATION OF ABSTRACT	18. NUMBER OF PAGES	19a. NAME OF RESPONSIBLE PERSON
a. REPORT	b. ABSTRACT	c. THIS PAGE			STI Help Desk (email: help@sti.nasa.gov)
U	U	U	UU	36	19b. TELEPHONE NUMBER *(Include area code)* (301) 621-0390